AD-A179 190 FINITE DIFFERENCE SIMULATIONS OF RAYLEIGH WAVE SCATTERING BY 2-D ROUGH TO..(U) TELEDYNE GEOTECH ALEXANDRIA VA K L MCLAUGHLIN ET AL. NOV 86 TGAL-86-9 1/1

UNCLASSIFIED AFGL-TR-86-0269 F19628-85-C-0035 F/G 8/11 NL

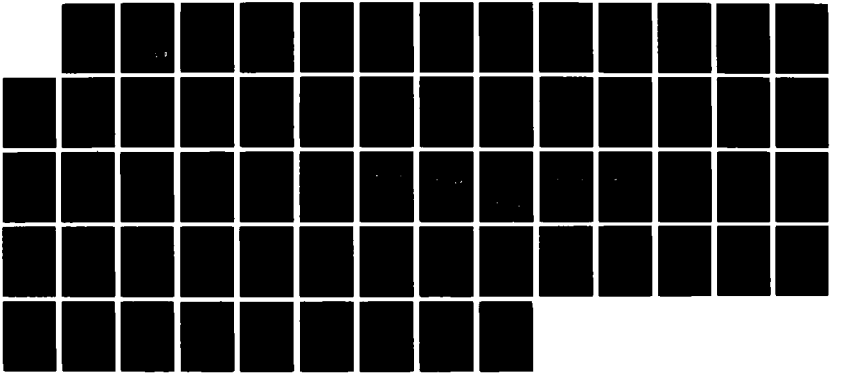

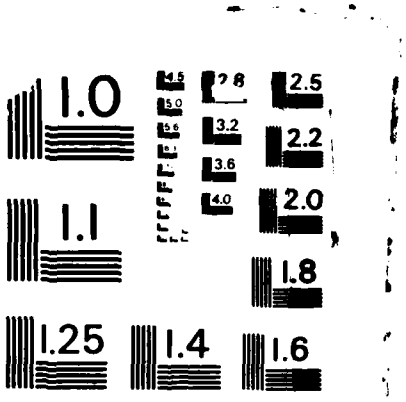

MICROCOPY RESOLUTION TEST CHART

NATIONAL BUREAU OF STANDARDS - 1963 - A

AFGL-TR-86-0269

Finite Difference Simulations of Rayleigh Wave Scattering by 2-D Rough Topography

K. L. McLaughlin
R. S. Jih

Teledyne Geotech
314 Montgomery Street
Alexandria, VA 22314

November 1986

Scientific Report No. 3

AIR FORCE GEOPHYSICS LABORATORY
AIR FORCE SYSTEMS COMMAND
UNITED STATES AIR FORCE
HANSCOM AIR FORCE BASE, MASSACHUSETTS 01731

DISCLAIMER NOTICE

THIS DOCUMENT IS BEST QUALITY PRACTICABLE. THE COPY FURNISHED TO DTIC CONTAINED A SIGNIFICANT NUMBER OF PAGES WHICH DO NOT REPRODUCE LEGIBLY.

UNCLASSIFIED
SECURITY CLASSIFICATION OF THIS PAGE

REPORT DOCUMENTATION PAGE

Form Approved
OMB No 0704-0188
Exp Date Jun 30, 1986

1a REPORT SECURITY CLASSIFICATION Unclassified	1b RESTRICTIVE MARKINGS
2a SECURITY CLASSIFICATION AUTHORITY	3 DISTRIBUTION / AVAILABILITY OF REPORT Approved for public release; distribution unlimited.
2b DECLASSIFICATION / DOWNGRADING SCHEDULE	
4 PERFORMING ORGANIZATION REPORT NUMBER(S) TGAL-86-9	5 MONITORING ORGANIZATION REPORT NUMBER(S) AFGL-TR-86-0269
6a NAME OF PERFORMING ORGANIZATION Teledyne Geotech 6b OFFICE SYMBOL (If applicable) TGAL	7a NAME OF MONITORING ORGANIZATION Air Force Geophysics Laboratory
6c ADDRESS (City, State, and ZIP Code) 314 Montgomery Street Alexandria, VA 22314	7b ADDRESS (City, State, and ZIP Code) Hanscom AFB MA 01731-5000
8a NAME OF FUNDING / SPONSORING ORGANIZATION Air Force Geophysics Laboratory 8b OFFICE SYMBOL (If applicable) DSO/GSD	9 PROCUREMENT INSTRUMENT IDENTIFICATION NUMBER F19628-85-C-0035
8c ADDRESS (City, State, and ZIP Code) Hanscom AFB MA 01731-5000	10 SOURCE OF FUNDING NUMBERS PROGRAM ELEMENT NO: 62714E PROJECT NO: 5A10 TASK NO: DA WORK UNIT ACCESSION NO: AX
11 TITLE (Include Security Classification) Finite Difference Simulations of Rayleigh Wave Scattering by 2-D Rough Topography	
12 PERSONAL AUTHOR(S) K.L. McLaughlin and R.S. Jih	
13a TYPE OF REPORT Scientific Report #3 13b TIME COVERED FROM _____ TO _____ 14 DATE OF REPORT (Year, Month, Day) November 1986 15 PAGE COUNT 60	
16 SUPPLEMENTARY NOTATION	

17 COSATI CODES			18 SUBJECT TERMS (Continue on reverse if necessary and identify by block number)
FIELD	GROUP	SUB-GROUP	Finite-Difference, Rayleigh Wave, Scattering, Coda, Topography, Q

19 ABSTRACT (Continue on reverse if necessary and identify by block number)

Rayleigh waves normally incident upon 2-D simple or rough topographic structures are simulated by the linear finite-difference method to study the attenuation, transmission, and reflection of Rayleigh waves and to measure the Rayleigh-to-P and -SV bodywave conversion. For simple ramp structures, transmission, reflection, and scattering depend on the sign of change of slope of the topographic feature, as well as the ratio of the ramp height to the wavelength, h/λ. Simple ramp structures produce back-scattered body-waves for $h > \lambda$, and forward-scattered body-waves for $h < \lambda$. The radiation patterns of P and S bodywaves are roughly consistent with the model of equivalent point forces along the free surface. More complicated topographic features generated by random Markov sequences have been characterized by the Rayleigh-wave spatial Q(f). As expected, rougher topography attenuates Rayleigh waves more than smooth topography. P and S amplitudes ratios are consistent with radiation from equivalent point forces near the surface, but the distribution of slownesses generated is

20 DISTRIBUTION / AVAILABILITY OF ABSTRACT ☒ UNCLASSIFIED/UNLIMITED ☐ SAME AS RPT ☐ DTIC USERS	21 ABSTRACT SECURITY CLASSIFICATION Unclassified
22a NAME OF RESPONSIBLE INDIVIDUAL James F. Lewkowicz	22b TELEPHONE (Include Area Code) (617) 377-3028 22c OFFICE SYMBOL LWH

DD FORM 1473, 84 MAR

83 APR edition may be used until exhausted
All other editions are obsolete

SECURITY CLASSIFICATION OF THIS PAGE
UNCLASSIFIED

(19. Continued)

greater than from the simple ramp structures. Reflection of Rayleigh waves by topographic slopes and by random topography is an inefficient process and the bulk of the energy that is not transmitted as Rayleigh waves is converted to bodywaves. Fundamental Rayleigh-to-Lg scattering and generation of teleseismic P coda by short period Rayleigh should be observable.

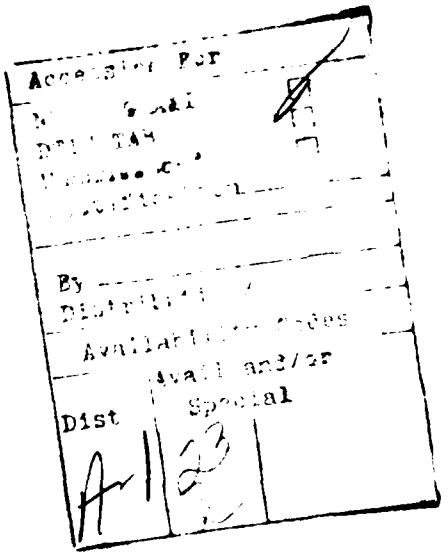

FINITE-DIFFERENCE SIMULATIONS OF RAYLEIGH WAVE SCATTERING BY 2-D ROUGH TOPOGRAPHY

SUMMARY

Rayleigh waves normally incident upon 2-D simple or rough topographic structures are simulated by the linear finite-difference method to study the attenuation, transmission, and reflection of Rayleigh waves and to measure the Rayleigh-to-P and -SV bodywave conversion. For simple ramp structures, transmission, reflection, and scattering depend on the sign of change of slope of the topographic feature, as well as the ratio of the ramp height to the wavelength, h/λ. Simple ramp structures produce back-scattered bodywaves for $h > \lambda$, and forward-scattered bodywaves for $h < \lambda$. The radiation patterns of P and S bodywaves are roughly consistent with the model of equivalent point forces along the free surface. More complicated topographic features generated by random Markov sequences have been characterized by the Rayleigh-wave spatial Q(f). As expected, rougher topography attenuates Rayleigh waves more than smooth topography. P and S amplitudes ratios are consistent with radiation from equivalent point forces near the surface, but the distribution of slownesses generated is greater than from the simple ramp structures. Reflection of Rayleigh waves by topographic slopes and by random topography is an inefficient process and the bulk of the energy that is not transmitted as Rayleigh waves is converted to bodywaves. Fundamental Rayleigh-to-Lg scattering and generation of teleseismic P coda by short period Rayleigh should be observable.

TABLE OF CONTENTS

INTRODUCTION

With some simple simulations we explore the stability of planar Rayleigh waves incident upon simple inclined surfaces and random rough topographic relief. We examine the reflected and transmitted Rayleigh waves as well as the bodywave field at depth as a measure of the simulated far-field P and S coda. In this way we characterize rough topography by a spatial Q for the transmitted Rayleigh waves and examine the partitioning of energy into bodywaves.

Since most previous research concerned with the scattering of Rayleigh waves has dealt with the simplest geometric configurations (quarter-space, three-quarter space, a trench or a vertical step) where the boundaries are always parallel or perpendicular to the grid axis, we have concentrated on the inclined surface and more general topographic profiles. Topographic scattering through a right angle step was addressed by deBremaecker (1958) and continues as a topic of interest. Numerous workers have examined the incident Rayleigh or Love wave upon welded quarter spaces (see for example Mal and Knopoff, 1965; McGarr and Alsop, 1967; Drake, 1972; Munasinghe and Farnell, 1973; Tuan and Li, 1974; Martel *et al.*, 1977; Sabina and Willis, 1977; Chen and Alsop, 1979; Fuyuki and Matsumoto, 1980; Drake and Bolt, 1980; Momoi, 1980, 1981, 1982; Fuyuki and Nakano, 1984; and Levander, 1985). Recent work has moved to more complicated geometries, 3-D as opposed to 2-D, or to more complicated structures. Ultrasonic modeling was used by Bullit and Toksoz (1985) to examine obliquely incident Rayleigh wave transmission and reflection by sloping topography. An important point made by Bullit and Toksoz was that the transmission coefficient is not phaseless and that there are phase shifts induced by the scattering. In a linearized theory of topographic scattering of surface waves, Sneider (1986) points out that the scattering loss is intimately related to the phase velocity perturbation induced by the topographic structure.

The problem of Rayleigh waves scattered by topography may have several applications. Short-period Rayleigh waves are sometimes observed from shallow earthquakes as well as from underground explosions. The scattering of such short-period Rayleigh waves by topography has been proposed as a mechanism for the generation of teleseismic P coda by Greenfield (1971). Gupta *et al.* (1986) have proposed that such P coda may be diagnostic of the near source medium. P coda observed at arrays is often partly composed of Rayleigh waves generated by P waves steeply incident upon shallow heterogeneity or topography. Key (1967, 1968) identified such Rayleigh waves within the P coda at the EKA array (Eskdalemuir, Scotland) for certain azimuths of arrival. Dainty (1986) shows by use of frequency-wavenumber analysis that P coda at the small NORESS array (southern Norway) is often composed of fundamental short-period Rayleigh waves. Both the coherency of such coda and its persistence are closely related to the scattering of the Rayleigh waves by topography and shallow heterogeneity. Aki and Chouet (1975) proposed three simple models for the generation and propagation of short-period coda from local earthquakes. They considered the case of scattered surface waves as well as scattered bodywaves. Although the coda of local earthquakes appears to be dominated by S waves, it is clear that trapped modes and surface waves are also present (Phillips and Aki, 1986). A portion of the regional Lg phase and its coda is composed of fundamental and higher mode Rayleigh waves trapped in the crustal waveguide. Der *et al.* (1984) propose that a significant portion of the Lg coda is composed of short-period fundamental Rayleigh waves that concentrate energy near the surface and are multiply scattered, contributing to the long Lg coda observed on regional seismograms. Baumgardt (1985) proposes that Lg from Eastern Kazakh incident upon the Urals produces observable teleseismic P coda at NORSAR. All of these problems have in common a need to estimate the effects of scattering on short-period surface waves due to shallow heterogeneity and topography.

In this paper we address the problem of transmission, reflection, and conversion of fundamental Rayleigh waves by topography on a homogeneous halfspace using two-dimensional linear elastodynamic finite differences. We first examine the problem of transmission through simple slopes and the partitioning of energy by the scattering process. It is demonstrated as expected that larger scale variations in topography produce larger coefficients of reflection and smaller transmission coefficients. Reflection is always observed to be an inefficient process. We have also observed that the reflection, transmission and diffraction are directional dependent. Both directionality and frequency dependence can be seen in the converted P and S bodywaves scattered from the topography. Next we examine the effective spatial Q produced by random topography. Attenuation of the short-period Rayleigh wave is found to be strong by moderate rough topography, and Rayleigh-to-bodywave conversion is seen to dominate the attenuation process.

THE FINITE-DIFFERENCE SCHEME

The 2-D linear finite-difference (LFD) scheme popularized by Kelly *et al.* (1976) is used with the Clayton and Engquist (1977) (Emerman and Stephen, 1983) absorbing boundary conditions on both the sides and the bottom of the grid. Even with the absorbing boundary conditions, the simulations are run with large enough grids such that for the duration of the simulations reflections from the sides do not seriously contaminate the results. The free-surface boundary conditions follow from the work of Jih *et al.* (1986) which allows for the introduction of arbitrary polygonal topography into the wave propagation simulations and has been applied by McLaughlin and Jih (1986) for the modeling of teleseismic P waves from explosive line sources under realistic topographic surfaces. These boundary conditions are extensions to those of Ilan (1975 and 1977). Recently a number of techniques have been pursued in an effort to improve the computational performance of LFD solutions to wave equations. These include variable grids, higher order schemes or implicit rather than explicit methods. We have found that none of these methods provide significant improvement over the traditional explicit second order centered LFD schemes described by Alterman, Boore and Kelly when rough topographic profiles are used at the free surface (Jih *et al.* 1986).

In the present experiments, the medium has P- and S-wave velocities of 5.0 and 2.96 km/sec respectively, corresponding to a Poisson's ratio of 0.35 and a Rayleigh wave velocity of 2.71 km/sec. The formulation generating the incident pure Rayleigh wave packet is analogous to Boore (1970) or Munasinghe and Farnell (1973) which has been used extensively by Martel *et al.* (1977), Fuyuki and Matsumoto (1980), Fuyuki and Nakano (1984), and Levander (1985). The initial waveform is the fundamental mode Rayleigh wave in the homogeneous half space with a Ricker wavelet shape (Figure 1). This method is superior to another

approach which shakes several mesh points on the free surface or the grid edge to generate the incident Rayleigh wave as well as undesirable bodywaves (Wojcik and Mak, 1985). To reduce the grid dispersion, we have oversampled the incident wave packet by choosing the dominant wavelength to be 3.2 km = 32 Δx, where Δx =0.1 km is the grid spacing.

NUMERICAL EXPERIMENTS: SIMPLE INCLINED SURFACES

Experiments were first conducted to justify that, in the case of a homogeneous half-space, the grid dispersion only modulates the spectra of the propagating Rayleigh wave (Figure 2). No significant attenuation of the Rayleigh wave could be measured for the half-space. Following this check, we introduced the simple ramp. We measured the transmission and reflection of Rayleigh waves incident upon simple uphill or downhill slopes with variable height. The reflection and transmission coefficients are dependent on the ratio of the ramp height to the wavelength as well as the direction of the ramp as shown in Table 1 for constant slope. For the same height, the downgoing slope always causes more reflection and less transmission as compared to the upgoing slope. Reflection is always less than transmission. For slopes of the same direction, larger scale variations in topography produce smaller transmission coefficients. Here we define the Rayleigh wave energy transmission coefficient, T, as $T(f) = \frac{Power_{trans}(f)}{Power_{inc}(f)}$. The reflection coefficient, R, is defined in an analogous way: $R(f) = \frac{Power_{refl}(f)}{Power_{inc}(f)}$. Power spectra of the strain (dilatation and rotation) were used to compute the coefficients so as not to be biased by the dispersion effects. The strain in each case was "measured" one grid point below the flat surface away from the slopes in question.

TABLE 1. Energy Transmission & Reflection Coefficients						
h/λ	uphill*			downhill*		
	T(1Hz)	R(1Hz)	1-T-R	T(1Hz)	R(1Hz)	1-T-R
1/16	.87	.01	.12	.75	.016	.22
1/4	.51	.003	.48	.44	.008	.55
1/2	.54	.004	.45	.16	.009	.83
1	.62	.0036	.38	.06	.035	.93
2	.22	.0033	.88	.034	.015	.95

*all ramps have 45° slope.

A significant conclusion is immediately apparent from Table 1, that the reflected energy and transmitted energy is far from 100% of the incident energy and that bodywave conversion must be very efficient. Clearly 55% of the Rayleigh wave energy is lost to bodywave conversion by passage down a $\lambda/4$ slope of 45°.

Figures 3 through 6 show snapshots of the displacement field due to a Rayleigh wave incident upon 45° ramps of various heights. Successive frames are separated by intervals of 2 seconds and the incident Rayleigh wave always travels from left to right. Displacements are proportional to the darkness of the plot and are normalized to the maximum in each frame. The diffraction pattern becomes much more complicated when the the height of the ramp is larger. This is obvious in comparing Figure 3 ($h = 0.5\lambda$) and Figure 5 ($h = 2\lambda$). In all cases the corners act as point sources radiating converted bodywaves (mainly S wave). When the incident Rayleigh wave encounters a rising hill, some energy is converted to P wave energy and propagates in essentially the same direction as the incident Rayleigh wave (Figure 6 and 8), while in the case of going down hill, the converted P wave scatters in all possible directions (Figures 3, 4, 5, and 7). In the case of the 2λ downhill slope, the amplitude spectral ratios of the forward scattered (with 30° takeoff angle) P- and S- waves over the backward scattered (with −30° takeoff angle) P- and S- waves near 1 Hz are 0.73 and 2.82 respectively. This is to say that the forward scattered P waves are 0.73 times as large as the back scattered P waves. The corresponding measurements in the case of going uphill are 1.4 and 1.3 for P

and S waves respectively. All these observations indicate that Rayleigh-to-bodywave conversion is directional dependent. Since Lg is dominated by S waves with a slowness corresponding to a takeoff angle in our simulation of about 30^o, we see that the Rayleigh-to-Lg conversion is preferentially in the forward direction by an average factor of 2 in amplitude (in this h = 2λ case).

Figure 7 and 8 show the snapshots of a Rayleigh wave incident upon a valley and a trapezoidal mesa of depth 1λ respectively. The scattering is dominated by the first corner or ramp encountered during the propagation and hence the diffraction pattern of the valley is very similar to that of single downgoing ramp (Figure 4). Likewise, the diffraction pattern of the mesa is similar to the upgoing ramp (Figure 6) as expected.

The transmitted and reflected Rayleigh waves can be seen in Figures 9A,B and 10A,B for the 2λ uphill and downhill cases. The amplitudes of these waves are in close agreement with the reflection and transmission coefficients determined from the power spectra.

When we examine the spectra of the forward- and back-scattered P and S waves, we find that we can separate the high- and low-frequency scattering regimes as, $\lambda < h$, and $\lambda > h$ respectively. From these simple observations we can compare the forward- and back-scattered P and S wavefields as a function of h/λ. The converted P waves are predominately forward scatter (about 10 times larger than the back scattered P waves) for $\lambda < h$, and more isotropic at low frequencies, for $\lambda > h$. This applies to Rayleigh waves converging on an uphill or downhill slope. In contrast, the converted S waves are roughly the same amplitude in the forward and backward directions for both high and low frequencies for Rayleigh waves incident on a downhill slope. The converted S waves from uphill slopes are dominated by forward-scattered waves at high frequencies, and dominated by back-scattered waves at low frequencies.

If we examine the P and S waves radiated by the ramps in Figures 3 through 6 and Figures 11 through 14, we see that there is an SV node in the vertical direction from each diffractor while the P wave radiation is of constant polarity. Intuitively, this follows from the retrograde elliptical P-SV motion of the incident Rayleigh wave. The fundamental mode has no shear strain component on a horizontal plane in the halfspace. This fundamentally influences the radiation patterns of the Rayleigh-to-body wave diffractors. The diffraction patterns resemble those of a point force directed in a direction bisecting the local normals at the corner. More SV energy will therefore tend to be trapped in the crustal waveguide and the P waves are more likely to escape the crustal waveguide at steeper angles of incidence.

Wavenumber spectra from the seismic sections of Figures 13 and 14 are shown for 1, 2, 3, and 4 Hz in Figures 15A,B and 16A,B. They indicate that most of the energy of both the P and S waves is steeply incident. The principle P and S waves go from steeply incident in the backward direction at 1 Hz to steeply incident in th forward direction as frequency increases from 1 to 4 Hz.

These experiments with simple topographic profiles are instructive since they show us that Rayleigh-to-bodywave conversion occurs near corners (changes in slope), is frequency dependent, directionally dependent, and in general depends on the sign in the change of slope. These phenomena are more difficult to observe in more complicated topographic profiles.

NUMERICAL EXPERIMENTS: ROUGH TOPOGRAPHIC PROFILES

In order to generate random topography, a random number generator is used to produce a Markov sequence of values 0, 1, or -1 with a chosen transition probability matrix. The associated random walk (integrated sequence) is then derived. The finite-difference scheme must discretize the topography into polygons, therefore the smallest scale length of the topography is always twice the horizontal grid spacing. The largest scale length is limited by the size of the grid used in the simulation. Several typical topographic profiles derived by this method are shown in Figures 17A through 17E.

15 rough topographic profiles were inserted into the grid with flat ground concatenated on both sides to simulate the propagation of Rayleigh waves across the grid. The initial incident waveform, the reflected and the transmitted waveforms were then measured at near surface "sensors" away from the rough topography. The grids are 26km in depth, with grid spacing of 0.1 km and widths between 34 to 39 km depending on the profile. Transmission coefficients and the attenuation factor Q(f) were then computed in the frequency domain. The results are shown in Figure 17A through 17E. The useful bandwidth is limited to frequencies below 4 Hz due to the limitation of 2nd order LFD scheme. Although we quote dimensions in km and velocities in km/s, it is possible to scale these simulations to higher or lower frequencies as desired.

Table 2 gives the statistics of several topographic profiles used and the corresponding attenuation factor Q at the dominant frequency. Here we computed the attenuation factor Q via $Q^{-1}(f) = -ln(T(f))(\frac{V_R}{2\pi fX})$. The *roughness coefficient* Ω_1 (or *normalized total variation*) is defined by $\Omega_1 \equiv \frac{\sum|H_i - H_{i-1}|}{X}$ where H_i is the elevation at ith column of the nontrivial por-

tion of the topography, X the traveling distance. This statistic reflects the idea that in a smooth sequence of points the differences between successive values are all small, and hence the numerator will be small. The denominator is simply a scaling factor. Further investigation on whether such Ω_1, as a measure of roughness, can characterize all general rough topographic features is necessary.

In these numerical tests, smoother topographic profiles have larger Q as expected. For the specific profiles listed in Table 2, the ordering is preserved if Ω_1 were replaced by the normalized l^2 norm of the elevation change, Ω_2, which is defined by $\frac{\sqrt{\sum(H_i-H_{i-1})^2}}{X}$. Q estimates are much the same whether shear or dilatational strain energy were used to measure attenuation. Several calculations were run at grid sizes differing by factors of 2 and 1.428. The resultant Q's were nearly identical.

TABLE 2. Rough Topographic Profiles

topography	span(km)	Ω_1	Q(.8Hz)*
3	8.7	.18	629
15	11.4	.39	184
5	11.9	.40	37
4	12.1	.46	33
10	11.5	.49	28
6	12.2	.52	25
11	11.2	.54	21
8	12.0	.58	15

* (V_R =2.71 km/s, λ =3.2km)

A horizontal array of 64 sensors are equally spaced near the bottom of the grid to record the converted P (dilatation) and SV (rotation) wavefields. Strain energy ratios were computed for the transmitted Rayleigh wave to the incident Rayleigh wave in order to estimate the

energy loss. Power spectra were used in order to avoid the dispersive effects of the scattering. Power ratio of the converted P (S) waves to the incident Rayleigh wave are used as a measure of scattering. Furthermore, a frequency-wavenumber analysis technique is used to produce F-K plots of the scattered dilatational and rotational bodywavefield as observed near the bottom of the grid.

Seismic sections from a linear array (Δx = 1 km) at depth within the grids for profiles #5, #10, and #15 are shown in Figures 18, 19 and 20. The P and S wavefields can be seen to be steeply incident upon the array from numerous point diffractors in the topographic profile. The coda lasts as long as it takes the Rayleigh wave to propagate across the profile. Wavenumber spectra from a linear array (Δx = 0.3 km) of sensors near the bottom of the grid are shown for profiles #5, #10, and #15 in Figures 21, 22, and 23. At 1 Hz, the wavenumber spectra show a broad pronounced maximum corresponding to nearly horizontally propagating P or S waves. The 1 Hz P and S waves are predominately back-scattered waves. At 2 Hz, the maximum broadens considerably and the forward-scattered waves are roughly equal in power to the back-scattered waves. The S wave spectra tend to show a notch near vertical incidence. At 3 and 4 Hz, the bodywaves are mostly forward-scattered waves.

The spectra of the bodywaves reflect the spatial attenuation of the Rayleigh wave. The strain energy partitioning between the P and S waves is approximately 1-to-10, when the areas under the wavenumber power spectra are accounted for. This is roughly independent of frequency. The amplitude ratio between the S and P waves is therefore roughly consistent with a ratio of $(\frac{\alpha}{\beta})^2$ as would be expected from a distribution of point forces rather than a ratio of $(\frac{\alpha}{\beta})^3$ as would be expected from a distribution of shear stresses at the surface. Recall that the P-to-S ratios from the simple 45° ramps were much smaller and had strong frequency dependence.

The relationship between the $Q^{-1}(f)$ and the wavenumber spectrum of the topography is not as clear as we would like. Table 2 shows a subset of Ω_1 versus Q for f = 0.8 Hz derived from several topographic profiles. However, another subset of random topographies were found to have a different relationship between the statistical moments and the Q at 0.8 Hz. We have plotted in Figure 10, the topographies, $H(x)$, their wavenumber spectra, $\hat{H}(k)$, and the estimated Q(f) for 15 different topographic realizations. Some of the statistics of these topographies are listed in Table 3 along with the Q's at 1, 2 and 3 Hz where Ω_1 and Ω_2 are defined as before, and $\Omega_3 \equiv \frac{\sum(H_i - H_{i-1})^2}{\sum(H_i - \bar{H})^2}$ with $\bar{H}$ the average elevation of the topography. Ω_3 is also called Durbin-Watson statistic or von Neumann ratio (*c.f.* Bloomfield, 1975).

TABLE 3. Rough Topographic Profiles

topography	Ω_1	Ω_2	Ω_3	Q(1Hz)	Q(2Hz)	Q(3Hz)
1	.40	.06	.0063	107	74	-
2	.25	.04	.16	75	54	-
3	.18	.05	.15	630	63	-
4	.46	.06	.012	44	33	-
5	.40	.06	.029	118	94	-
6	.52	.07	.024	23	27	-
7	.47	.06	.0084	19	27	121
8	.58	.07	.012	13	31	91
9	.42	.06	.0096	24	36	-
10	.49	.07	.013	30	36	-
11	.54	.07	.012	23	36	-
12	.41	.06	.08	211	71	-
13	.41	.06	.08	100	57	-
14	.42	.06	.023	97	80	-
15	.39	.06	.041	104	49	-

DISCUSSION AND CONCLUSIONS

We see that moderate topography on a half space can substantially attenuate a short-period fundamental Rayleigh wave. A substantial portion of the energy is lost to bodywave conversion. We can expect to see P and S waves radiated as coda to teleseismic distances by short-period fundamental Rayleigh waves and some P-SV energy trapped in the crustal waveguide as Lg. A significant result of the topographic simulations is that reflection of Rayleigh waves by topography at normal incidence is very inefficient. Therefore we should not expect to see Rayleigh back-scattering as a significant contributor to the multiple scattering of fundamental Rayleigh waves that populate P coda.

We have performed the 2-D numerical Rayleigh-wave scattering experiments both upon simple ramps as well as more complicated random topographies. The simple ramps show that reflection is an inefficient process and that the bulk of the energy that is not transmitted across a step is converted to bodywaves. The transmission through a step is frequency dependent and depends on the direction of the step. The bodywaves appear to radiate from the changes in slope and to first order can be visualized as from a point force diffractor. The S waves have a null in the direction of the local normal similar to the radiation pattern of a vertical point force. At low frequencies ($h < \lambda$), the bodywaves are predominately back-scattered, while at high frequencies ($h > \lambda$), there is a predominance of forward-scattering.

More complicated topographic profiles contain many scale lengths and introduce broad-band effects. The Rayleigh wave attenuation is a complicated function frequency but is a maximum in the range where the wavenumber spectra of the topography matches the wavelength of the incident Rayleigh wave.

The uncertainties in the Q estimates are often approaching 100% for the Q^{-1} values less than 0.01 in Figure 17. A expected, the lowest Q's are always the best determined. When several topographic profiles are selected from an ensemble with the same statistics we see that the Q also has a characteristic variance. For example, the four profiles #12, #13, #14, and #15 were generated by using different seeds and have similar spectra and Q(f) with an average Q of 90 in the 1 to 2 Hz band with a standard deviation of 30%.

The dilatational and rotational wavenumber spectra indicate that the scattered P and S waves are scattered in the backward direction at low frequencies (1 Hz) and in the forward direction at high frequencies (4 Hz). Since the profiles are band-limited, $\lambda <$ total span and $\lambda > 0.2$ km, the intermediate frequencies (1 to 3 Hz) are probably the most reliable ($0.9 \leq \lambda \leq 2.7$). In this bandwidth, we see that the ratio of the P-to-S waves is nearly constant with a value near $(\frac{\alpha}{\beta})^2$ as if the apparent source were a distribution of point forces, and the scattering is a mixture of forward- and back-scattering. While apparently more SV energy may be trapped in the crustal waveguide, the clearly defined node in the vertical direction is less well defined for random rough topography and the SV energy is more evenly distributed in takeoff angle or slowness.

The results presented offer a beginning approach to effects of scattering by topography and heterogeneity upon surface waves. We have assumed that topography can be approximated by level elevations separated by sections of 45° slope. Our principle limitation is that we require segments of topography to exceed $2\Delta x$ (Jih *et al.*, 1986) and that Δx must be less than $\lambda/30$ (Fuyuki and Matsumoto,1980). A complete exploration of the problem will require variation of the P and S velocities, near surface velocity gradients, as well as crustal velocity heterogeneity. The short-period Rayleigh will not efficiently propagate across rough topography and reflection is small. Unless other mechanisms are found to trap P-SV energy within the

crust, the bulk of the energy will leak out of the waveguide. This can be mitigated by lowering the near surface velocity to spread the slowness space available to the converted P and SV waves, increasing the $\frac{\alpha}{\beta}$ ratio, introduction of gradients near the surface to create higher order modes, and/or velocity heterogeneity to scatter P and SV energy back into the waveguide. In short, all these mechanisms can only increase the Rayleigh-to-Lg coupling.

ACKNOWLEDGEMENTS

We would like to thank Z. A. Der, T. McElfresh, and L. M. Anderson for some of the initial programming efforts that led to successful application of Rayleigh waves incident upon topographic structures. This work was supported by the Defense Advanced Projects Agency and monitored by the Air Force Geophysics Laboratory under contract F19628-85-C-0035. The views and conclusions contained in this work are those of the authors and should not be interpreted as necessarily representing the official policies, either expressed or implied, of the Defense Advanced Research Projects Agency or the U.S. Government.

REFERENCES

Aki, K., Chouet, B. (1975), Origin of coda waves: source, attenuation, and scattering effects, *J. Geophys. Res.* **80,** 3322-3342.

Baumgardt, D. R. (1985), Comparative analysis of teleseismic P coda and Lg waves from underground nuclear explosions in Eurasia: *Bull. Seism. Soc. Am.*, **75,** 1413-1434

Bloomfield, P., 1975, *Fourier Analysis of time series: an introduction* , John Wiley & Sons, Inc.

Boore, D. (1970), Love waves in nonuniform wave guides: finite-difference calculations: *J. Geophy. Res.*, **75,** 1512-1527,

deBremaecker, J. Cl. (1958), Transmission and reflection of Rayleigh waves by corners, *Geophysics*, **23,** 1701-1731.

Bullit, J. T., Toksoz, M.N. (1985), Three-dimensional ultrasonic modeling of Rayleigh wave propagation: *Bull. Seism. Soc. Am.*, **75,** 1087-1104.

Chen, T. C. and L. E. Alsop, (1979), Reflection and transmission of obliquely incident Rayleigh waves at a vertical discontinuity between two welded quarter-spaces, *Bull. Seism. Soc. Am.*, **69,** 1409-1423.

Clayton, R., Engquist, B. (1977), Absorbing boundary conditions for acoustic and elastic wave equations: *Bull. Seism. Soc. Am.*, **67,** 1529-1540.

Clayton, R. W., Harkrider, D. G., Helmberger, D. V. (1986), Body and surface wave modeling of observed seismic events: *AFGL-TR-86-0021, Semi-Annual Report # 1*, California Institute of Technology, Pasadena, CA 91125. ADA169413

Dainty, A. M. (1986), Coda observed at NORSAR and NORESS, *AFGL-TR-85-0199, Final Report* Georgia Tech Research Institute, Atlanta, GA 30323. ADA166454

Der, Z. A., Marshall, M. E., O'Donnell, A., McElfresh, T. W. (1984), Spatial coherence structure and attenuation of the Lg phase, site effects, and the interpretation of the Lg coda: *Bull Seism. Soc. Am.*, **74,** 1125-1147.

Drake, (1972), Love and Rayleigh waves in nonhorizontally layered media: *Bull. Seism. Soc Am* , **62,** 1241-1258.

Drake, (1972), Rayleigh waves at a continental boundary by the finite element method: *Bull Seism. Soc. Am* , **62,** 1259-1268.

Drake, L. A. and B. A. Bolt, (1980), Love waves normally incident at a continental boundary, *Bull Seism Soc. Am. 70*, 1103-1123.

Emerman, S., Stephen, R. (1983), Comment on "Absorbing boundary conditions for acoustic and elastic wave equations," by R. Clayton and B. Engquist, *Bull. Seism. Soc. Am.*, **73**, 661-665.

Fuyuki, M., Matsumoto, Y. (1980), Finite-difference analysis of Rayleigh wave scattering at a trench: *Bull. Seism. Soc. Am.*, **70**, 2051-2069.

Fuyuki, M., Nakano, M. (1984), Finite-difference analysis of Rayleigh wave transmission past an upward step change: *Bull. Seism. Soc. Am.*, **74**, 893-911.

Greenfield, R. J. (1971), Short-period P-wave generation by Rayleigh-wave scattering at Novaya Zemlya: *J. Geophys. Res.*, **76**, 7988-8002.

Gupta, I. N., Blandford, R. R., A study of P waves from NTS explosions: near-source information from teleseismic observations? *Bull. Seism. Soc. Am.*, (to appear).

Hudson, J. A. (1967), Scattered surface waves from a surface obstacle: *Geophys. J. R. astr. Soc.*, **13**, 441-458.

Ilan, A., Ungar, A., Alterman, Z. (1975), An improved representation of boundary conditions in finite-difference schemes for seismological problems: *Geophys. J. R. astr. Soc.*, **43**, 727-745.

Ilan, A. (1977), Finite-difference modeling for P-pulse propagation in elastic media with arbitrary polygonal surface: *J. Geophys.*, **43**, 41-58.

Jih, R.-S., McLaughlin, K. L., Der, Z. A. (1986), Boundary conditions for arbitrary polygonal topography in elastic finite-difference scheme for seismogram generation, *TGAL*–86–03, Teledyne Geotech, Alexandria, VA 22314. Section I of Report AFGL-TR-86-0159.

Kelly, K. R., Ward, R. W., Treitel, S., Alford, M. (1976), Synthetic seismograms: a finite-difference approach: *Geophysics*, **41**, 2-27.

Key, F. A. (1967), Signal-generated noise recorded at Eskdalemuir seismometer array station: *Bull. Seism. Soc. Am.*, **57**, 27-37.

Key, F. A. (1968), Some observations and analyses of signal generated noise: *Geophys. J. R astr. Soc.*, **15**, 377-392.

Levander, A. (1985), Finite-difference calculations of dispersive Rayleigh wave propagation: *Tectonophysics*, **113**, 1-30.

Mal, A. K., Knopoff, L. (1965), Transmission of Rayleigh waves past a step change in elevation: *Bull. Seism. Soc. Am.*, **55**, 319-334.

Martel, L., Munasinghe, M., Farnell, G. W. (1977), Transmission and reflection of Rayleigh wave through a step: *Bull. Seism. Soc. Am.*, **67**, 1277-1290.

McGarr, A. and L. E. Alsop, (1967), Transmission and reflection of Rayleigh waves at vertical boundaries, *J. Geophys. Res.*, **72,** 2169-2180.

McLaughlin, K. L., Jih, R.-S. (1986), Scattering from near-source topography: teleseismic observations and numerical 2-D explosive line source simulations, *TGAL–86–03*, Teledyne Geotech, Alexandria, Virginia 22314. Section III of Report AFGL-TR-86-0159.

Momoi, T. (1980), Scattering of Rayleigh waves in an elastic quarter space: *J. Phys. Earth*, **28,** 385-413.

Momoi, T. (1981), Scattering of Rayleigh wave at a vertical boundary: *J. Phys. Earth*, **29,** 435-485.

Momoi, T. (1981), Scattering of Rayleigh waves by a rectangular rough surface: *J. Phys. Earth*, **30,** 295-319.

Munasinghe, M., Farnell, G. (1973), Finite-difference analysis of Rayleigh wave scattering at vertical discontinuities: *J. Geophy. Res.*, **78,** 2454-2466.

Phillips, S. W., Aki, K. (1986), Site amplification of coda waves from local earthquakes in central California: *Bull. Seism. Soc. Am.*, **76,** 627-648.

Sabina, F. J., Willis, J. R., (1977), Scattering of Rayleigh waves by a ridge: *J. Geophys.* **43,** 401-419.

Sneider, R. (1986), Phase speed perturbations and three-dimensional scattering effects of surface waves due to topography: *Bull. Seism. Soc. Am.*, **76,** 1385-1392.

Toksoz, M. N., Dainty, A. M., Charrette, E. E. (1986), Development of ultrasonic modeling techniques for the study of seismic wave scattering due to crustal inhomogeneities, *AFGL-TR-86-0078, Final Report.* Earth Resources Laboratory, MA 02139.

Toksoz, M. N. (1983), Development of ultrasonic modeling techniques for the study of crustal inhomogeneities, *AFGL-TR-83-0070, Final Report.* Earth Resources Laboratory, MA 02139. ADA134501

Tuan, H. S., Li, R. C. M. (1974), Rayleigh-wave reflection from groove and step discontinuities: *J. Acoust. Soc. Am.*, **55,** 1212-1217.

Wojcik, L. W., Mak, R. (1985), A numerical study of diffraction in reentrant geologic structure: *AFGL-TR-85-0158, Scientific Report #1.* Weidlinger Associates, Palo Alto, CA. ADA168562

FIGURE CAPTIONS

Figure 1A Wavenumber spectrum $S(k) = (k/k_0)^2 exp[1-(k/k_0)^2]$ of Ricker wavelet where k is wavenumber and $k_0 = 1.963$ radians/km the maximum amplitude wavenumber.

Figure 1B Ricker wavelet in the spatial domain. IFFT was applied on $S(k)$ to speed up the wavelet generation.

Figure 1C Rayleigh wave displacement eigenfunctions for the vertical and horizontal components of motion.

Figure 2 Spectral ratio of the transmitted Rayleigh waves over the incident Rayleigh waves in a homogeneous half-space. Grid dispersion only modulates the spectra.

Figure 3 The snapshots of the displacement field due to Rayleigh wave incident on a 45-degree ramp of height $h = 0.5\ \lambda$. Successive frames, A through F, are separated by 2 sec intervals. Displacements are proportional to the darkness of the plot and are normalized to the maximum in each frame. Note the P and S waves generated by the two corners of the ramp.

Figure 4 Same as Figure 3 except $h = \lambda$. The diffracted wavefield is more complicated as compared to the case $h = 0.5\ \lambda$ (Figure 3). There is a minimum in the scattered S wave in the near vertical direction.

Figure 5 Same as Figure 3 except $h = 2\ \lambda$. The diffracted wavefield is more complicated as compared to the cases of smaller h (Figure 3 and 4) or the case of upgoing cliff with the same height (Figure 6). Note the constructive interference of the forward-scattered S wave by the two corners and destructive interference for the back-scattered S wave.

Figure 6 Same as Figure 5 except the direction of the ramp is reversed. Note that the diffracted P and S waves propagate mainly to the right while for downgoing ramps (Figure 3, 4, 5) or valley (Figure 7) the diffracted bodywaves propagate more isotropically.

Figure 7 Rayleigh wave incident upon a valley of depth $1\ \lambda$. The scattering is dominated by the first downgoing ramp encountered during the propagation and hence the diffraction pattern is very similar to Figure 4.

Figure 8 Rayleigh wave incident upon a trapezoidal mesa of height $1\ \lambda$. The high-frequency fraction of the Rayleigh wave propagates along the mesa surface while the low-frequency fraction tunnels through the mesa.

Figure 9A Synthetic near-surface vertical displacements (upper) and horizontal displacements (below) for a Rayleigh wave incident on a 2λ deep downhill. Location of sensors are shown in Figure 5A. Note the phase dispersion of the transmitted Rayleigh wave. Two reflected waves are seen from each of the two corners.

Figure 9B Synthetic near-surface dilatational strain (upper) and rotational strain (below) for a Rayleigh wave incident on a 2λ deep downhill. Location of sensors are shown in Figure 5A.

Figure 10A Same as 9A except for opposite direction of the ramp. Location of sensors are

shown in Figure 6A.

Figure 10B Same as 9B except for opposite direction of the ramp. Location of sensors are shown in Figure 6A.

Figure 11 Seismic sections recording the converted P wave (dilatational strain, upper) and S wave (rotational strain, lower) at a line of 32 sensors near the bottom of the grid spaced 1 km apart for the case of 0.5λ deep downhill. See Figure 3.

Figure 12 Same as 11 except for opposite direction of the ramp. See Figure 4.

Figure 13 Same as 11 except for 2λ deep downhill. See Figure 5.

Figure 14 Same as 12 except for opposite direction of the ramp. See Figure 6.

Figure 15A Log-power horizontal wavenumber spectra for the dilatational wavefield recorded across the bottom linear array for the 2λ downgoing ramp case. Power spectra at 1, 2, 3, 4Hz are normalized to the maximum. Normally incident waves have a horizontal wavenumber of zero. Wavenumbers are indicated for horizontally propagating P waves. Forward-scattered waves have negative wavenumbers, back-scattered waves have positive wavenumbers. Note that the dilatational power is confined to steep angles of incidence across the array, slightly back-scattered at 1 Hz, and more isotropic at 4 Hz.

Figure 15B Log-power wavenumber spectra for the rotational wavefield recorded across the bottom of the grid for the 2λ downgoing ramp case. S waves are back-scattered with steep angle of incidence at 1 Hz and more isotropic at 4 Hz but still steeply incident.

Figure 16A Same as 15A except for opposite direction of the ramp.

Figure 16B Same as 15B except for opposite direction of the ramp.

Figures 17A,B,C,D,E Topography, $H(x)$, on the left, log-amplitude wavenumber spectra of the topography in the center, and the estimated Rayleigh-wave log(1/Q(f)) on the right for topographic profiles #1 through #15.

Figure 18 Seismic sections recording the converted P wave (dilatational strain, upper) and S wave (rotational strain, below) at a line of 32 sensors located near the bottom of the grid spaced 1 km apart for rough topography #5. Complicated interference patterns are evident for both P and S wavefields.

Figure 19 Same as 18 except for rough topographic profile #10.

Figure 20 Same as 18 except for rough topographic profile #15.

Figure 21A Frequency wavenumber spectra for the dilatational strain field (P-wave) recorded near the bottom of the grid with topography #5 on the top of the grid. The dilatational strain energy is largely confined to P wave slowness across the array. P wave energy shifts from back-scattered to forward-scattered from 1 to 4 Hz.

Figure 21B Frequency wavenumber spectra for the rotational strain field (S-wave) recorded near the bottom of the grid with topography #5 on the top. The rotational strain energy is largely confined to S wave slowness across the array. S wave energy shifts from back-scattered to forward-scattered from 1 to 4 Hz.

Figure 22A Same as 21A except for rough topographic profile #10.

Figure 22B Same as 21B except for rough topographic profile #10.

Figure 23A Same as 21A except for rough topographic profile #15.

Figure 23B Same as 21B except for rough topographic profile #15.

A

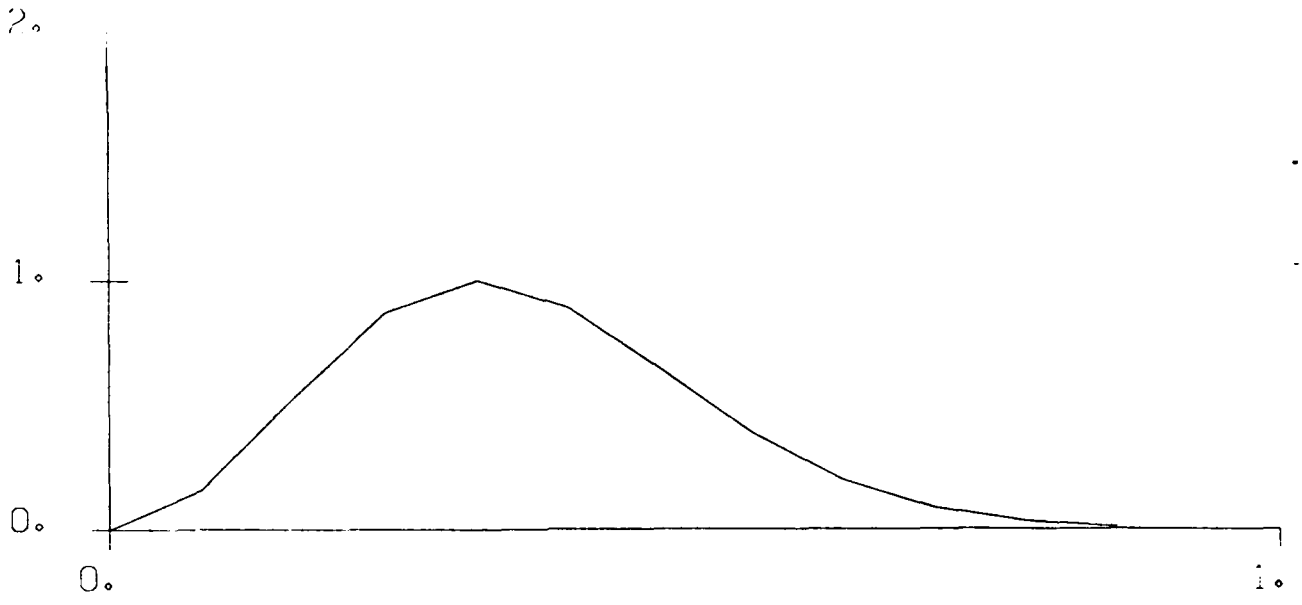

B

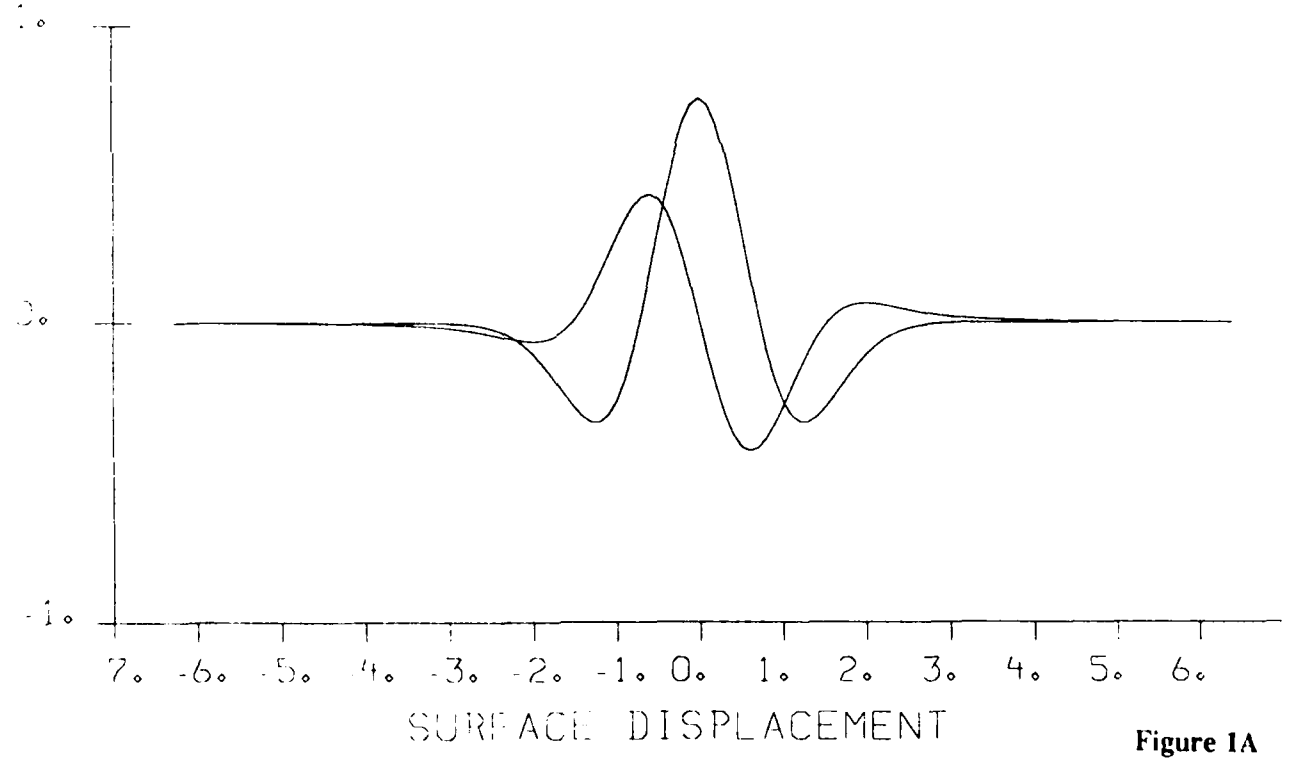

Figure 1A

Figure 1B

C

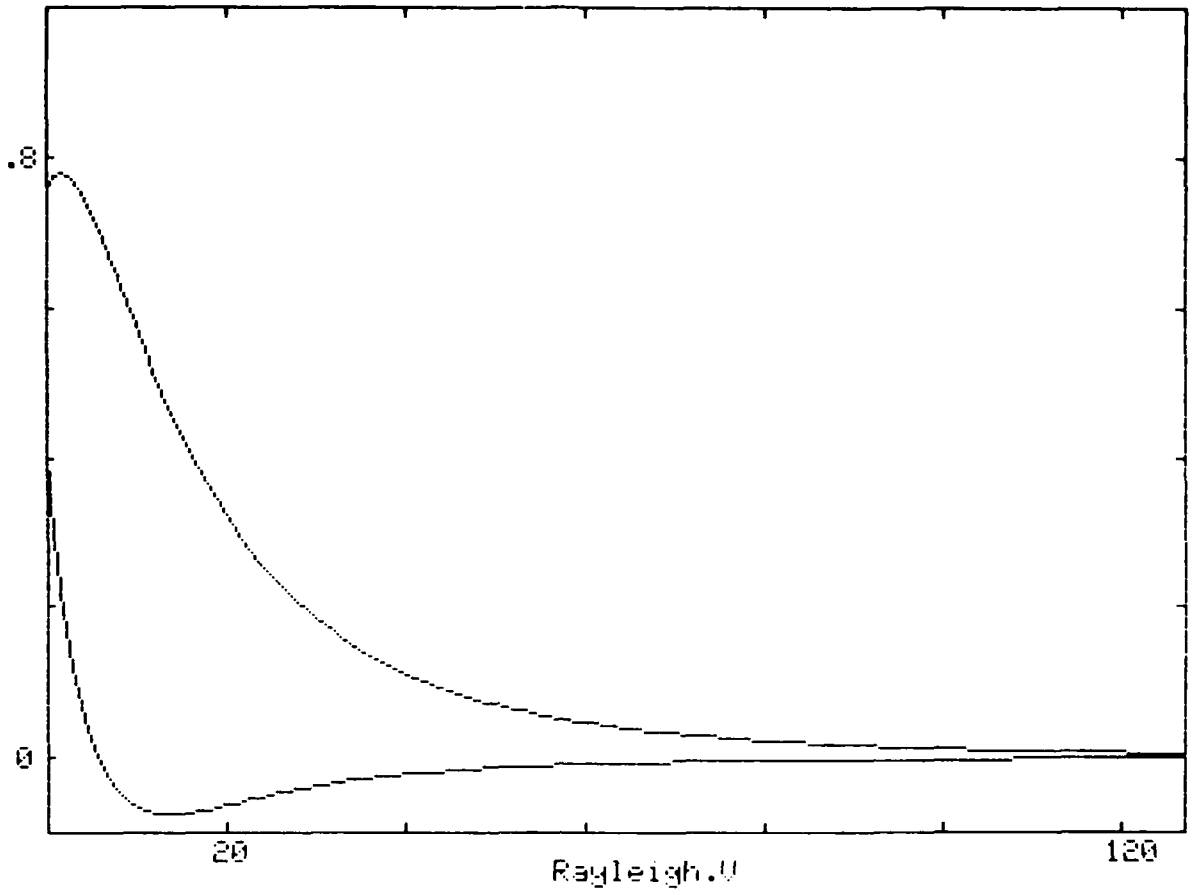

Figure 1C

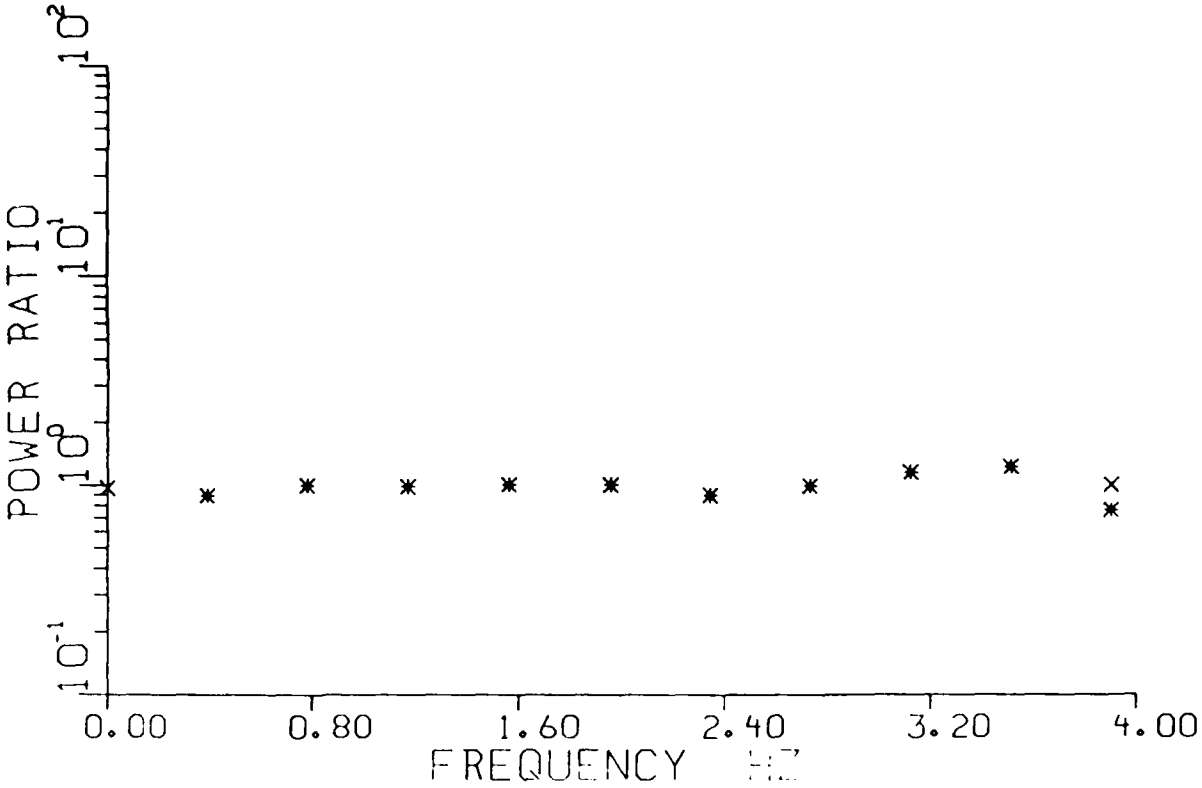
POWER RATIO
10^{2}
10^{1}
10^{0}
10^{-1}
0.00
0.80
1.60
2.40
3.20
4.00
FREQUENCY HZ

Figure 2

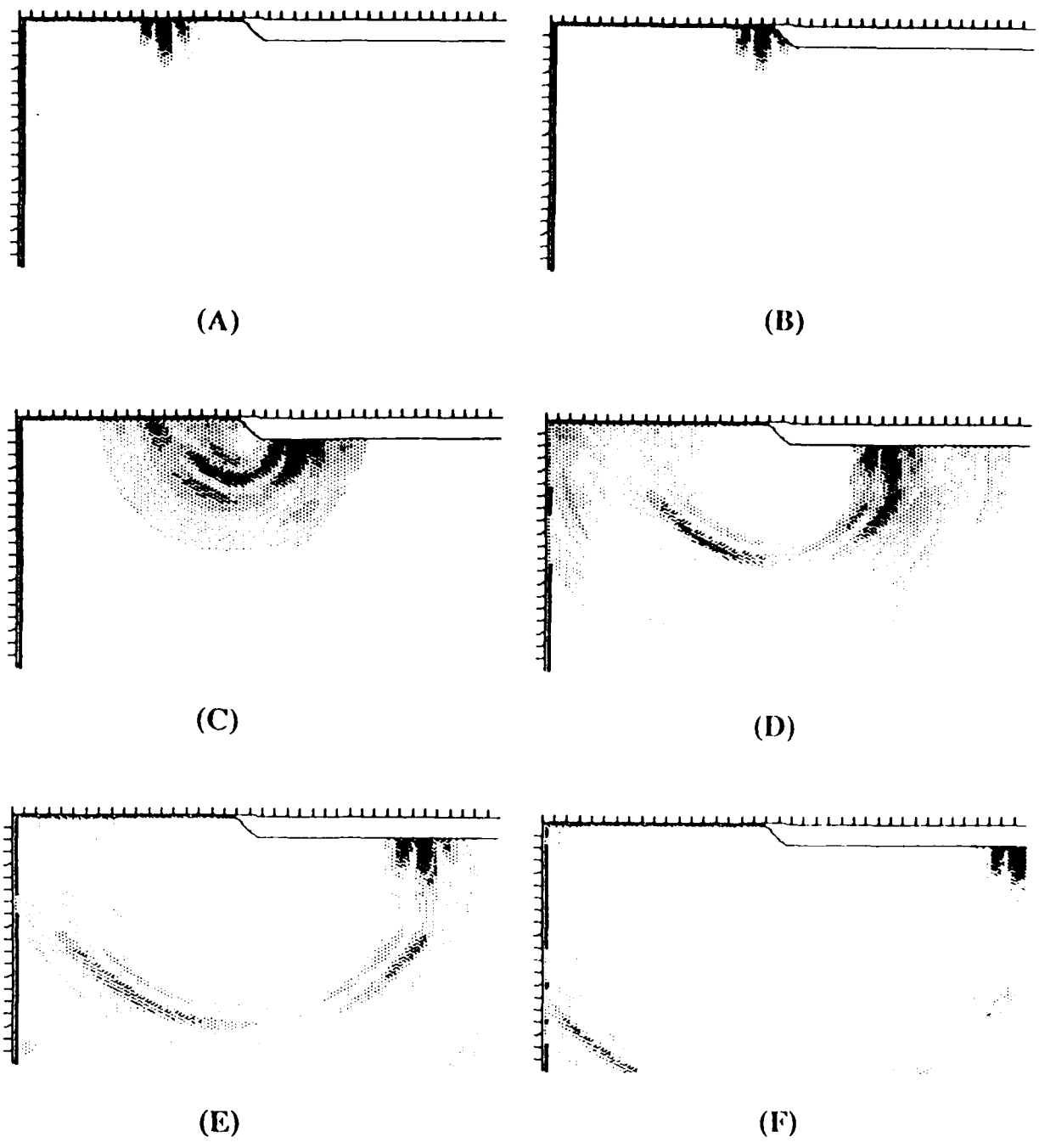

Figure 3

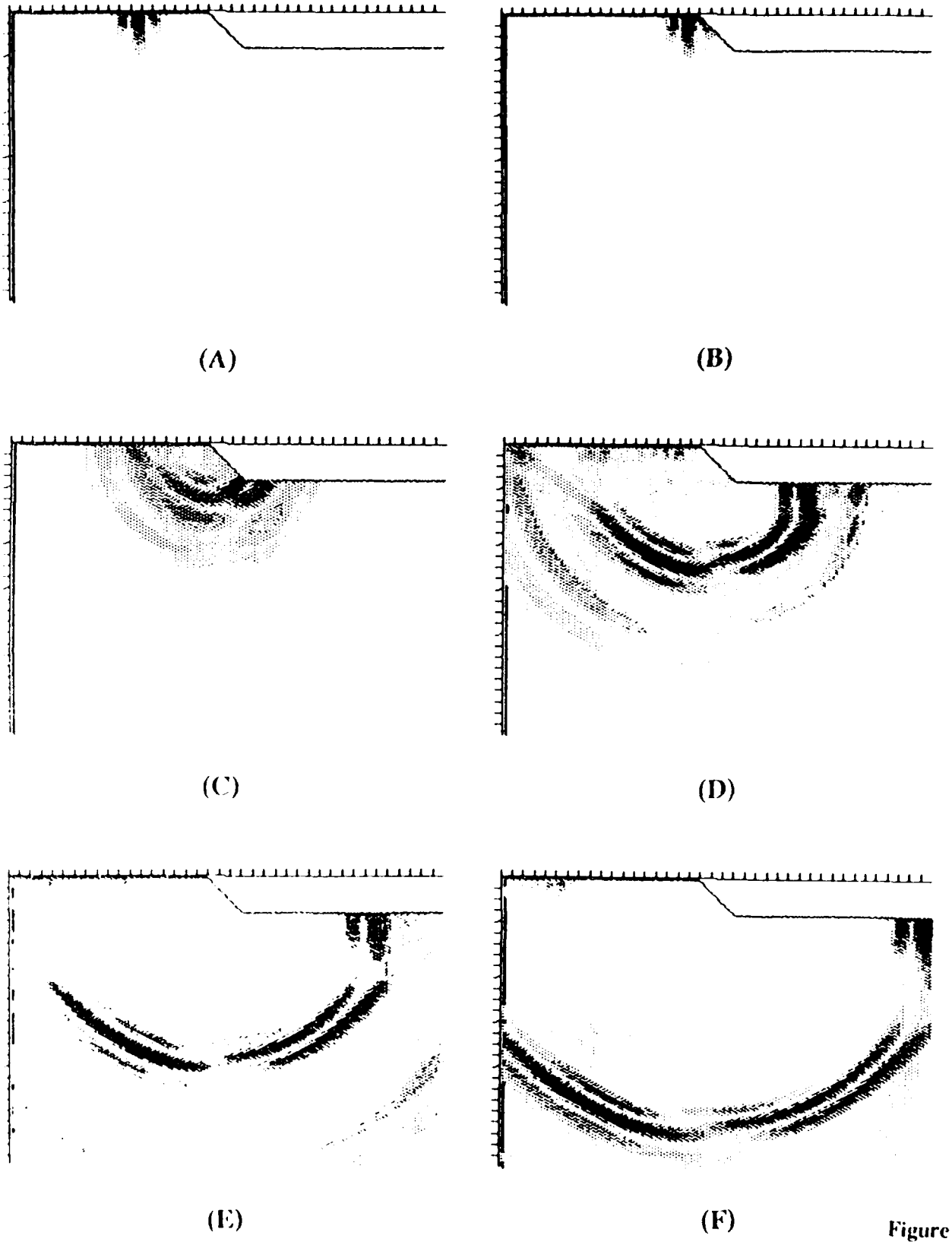

Figure 4

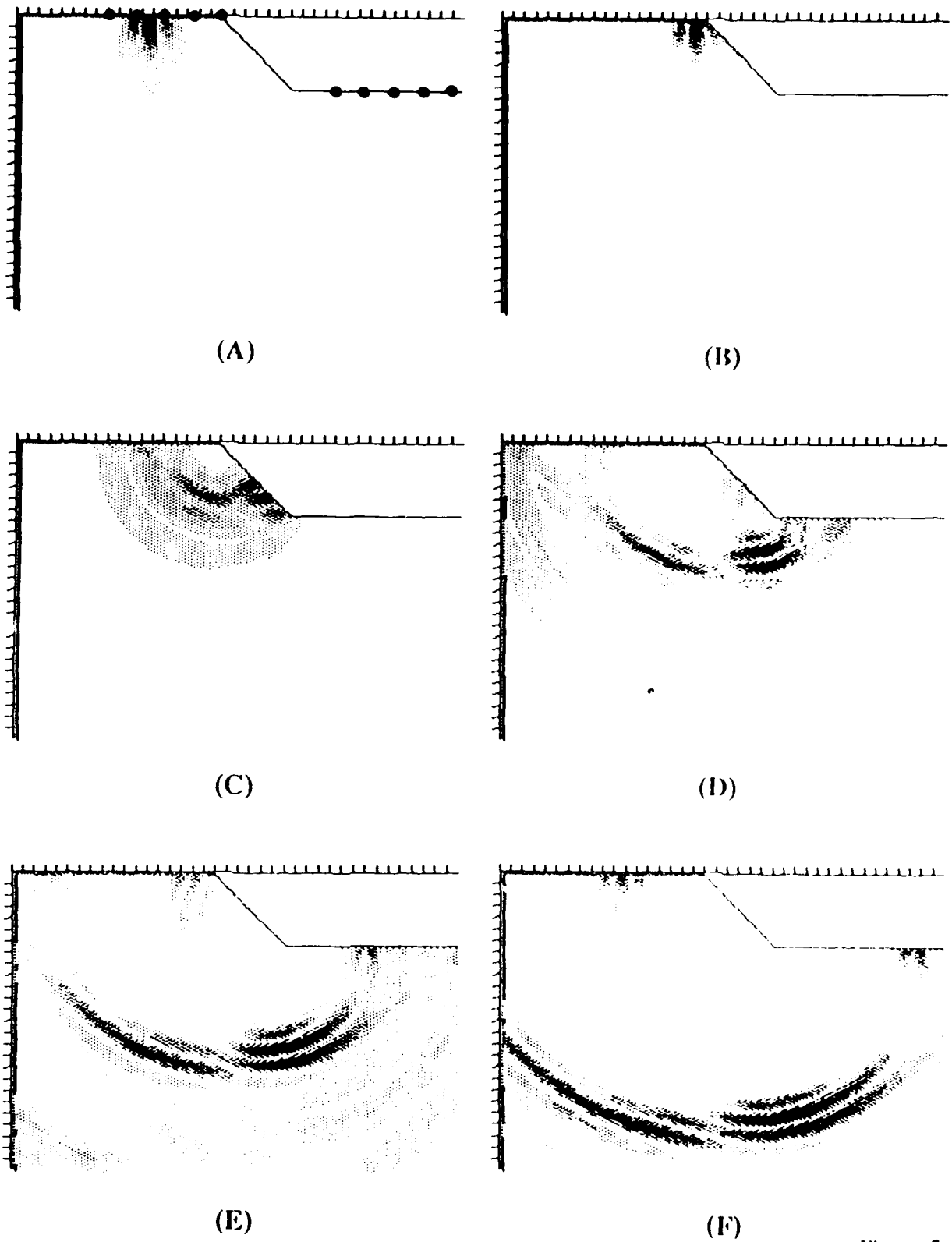

Figure 5

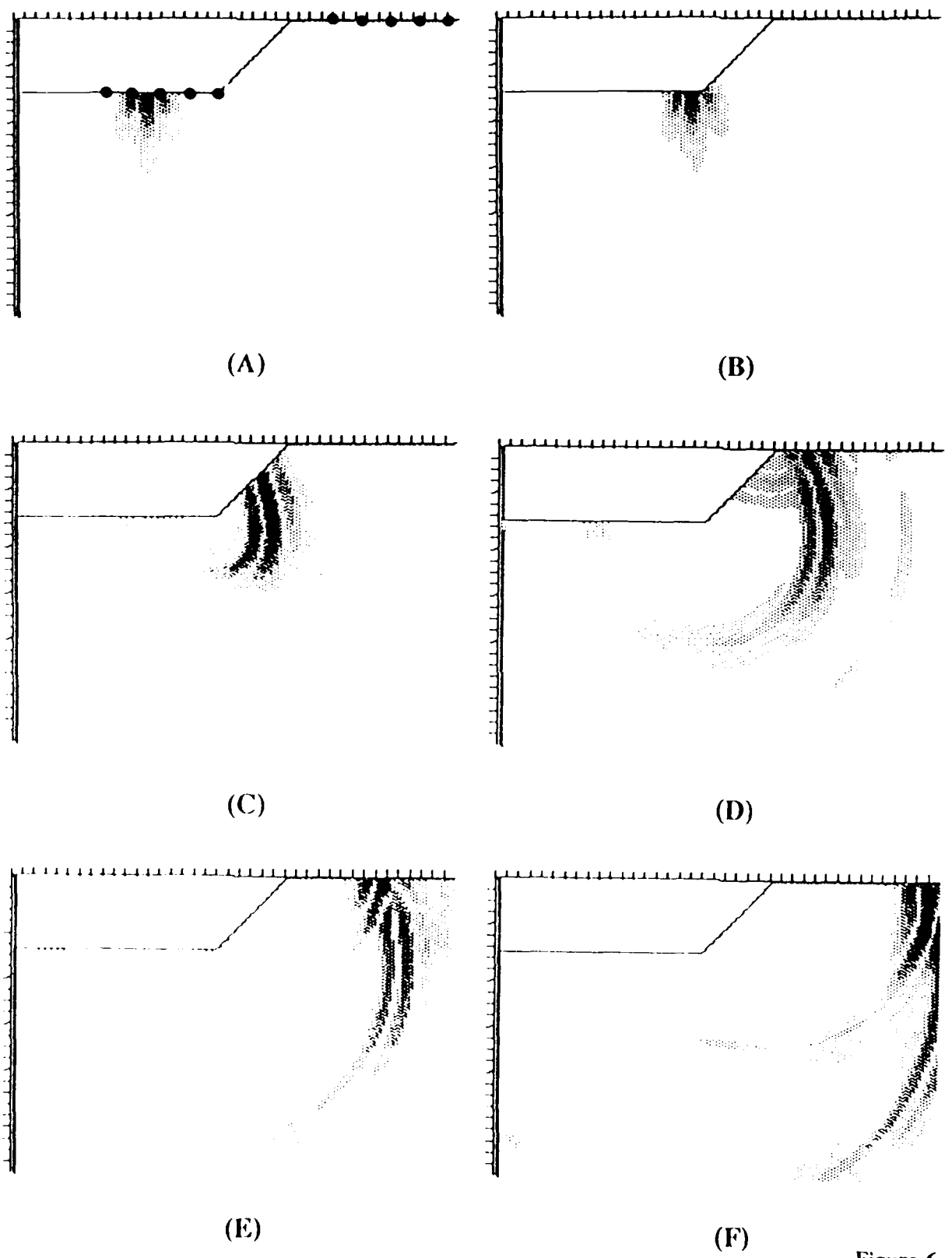

Figure 6

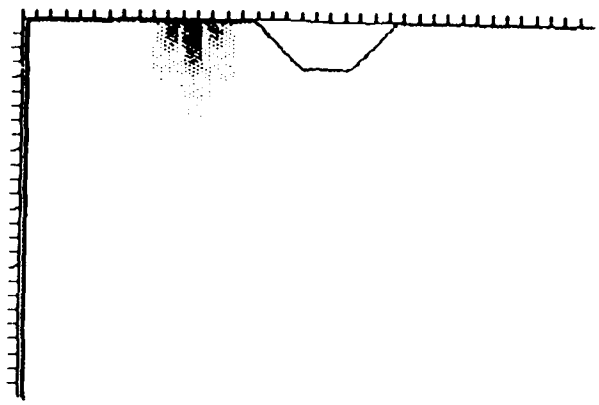

(A)

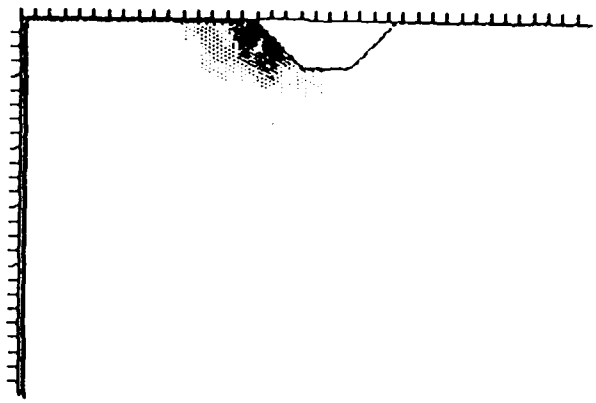

(B)

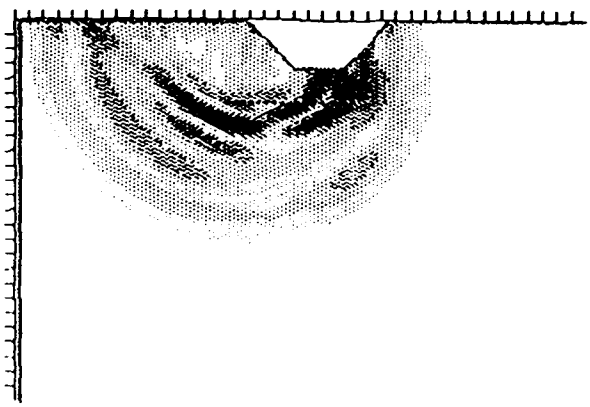

(C)

(D)

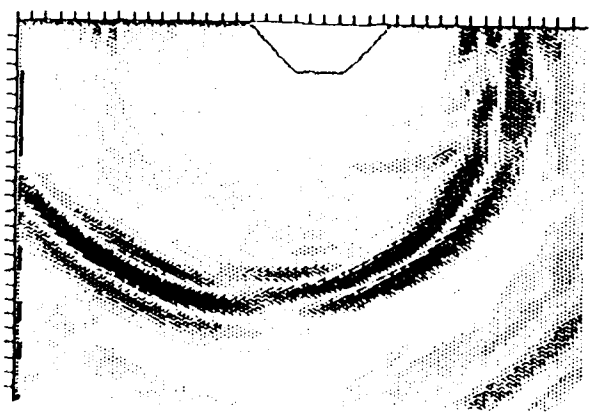

(E)

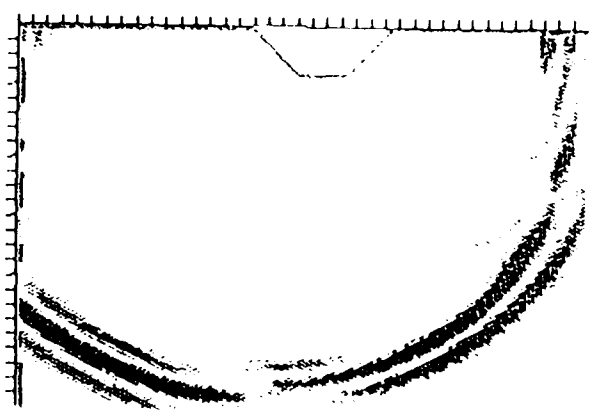

(F)

Figure 7

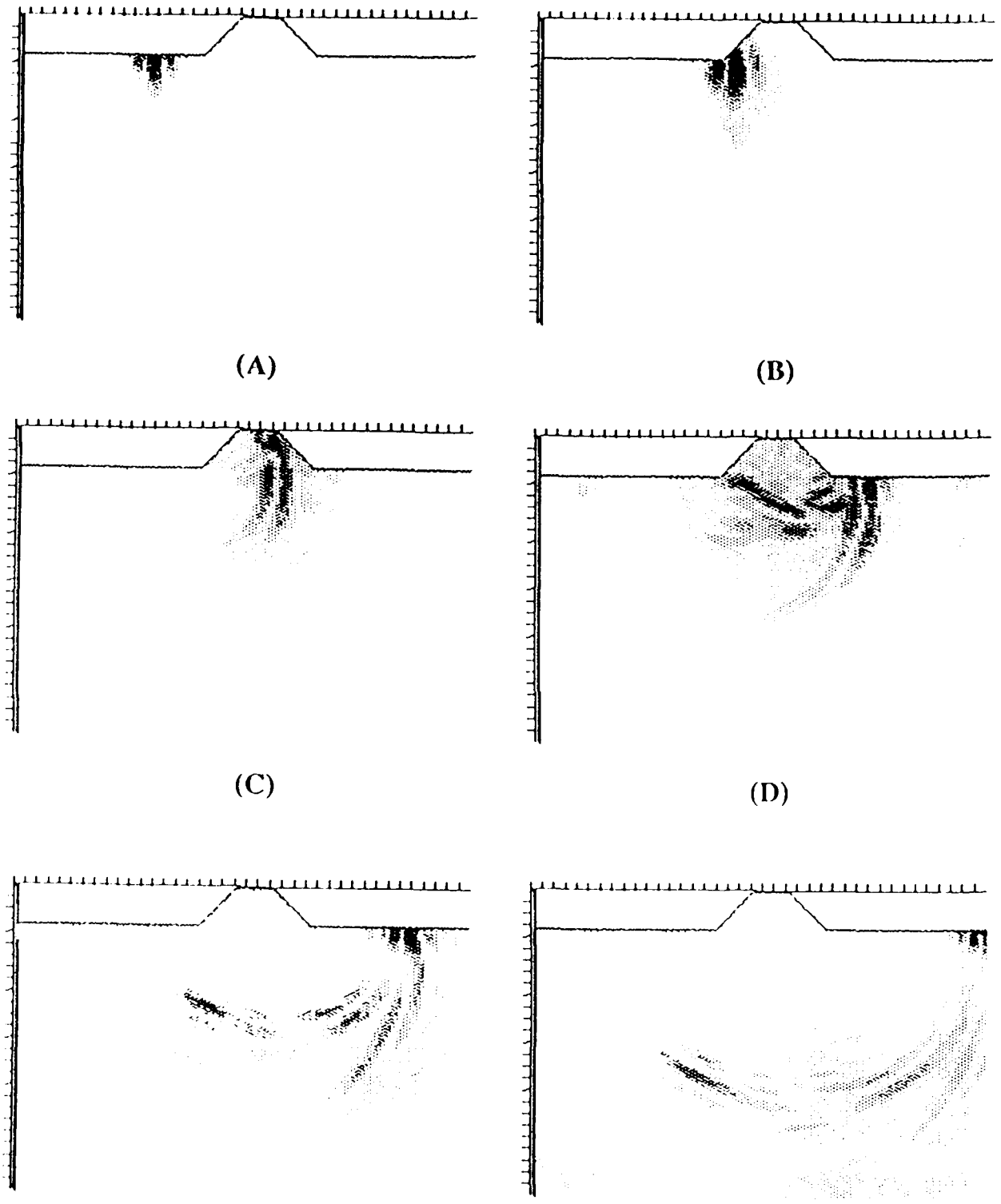

Figure 8

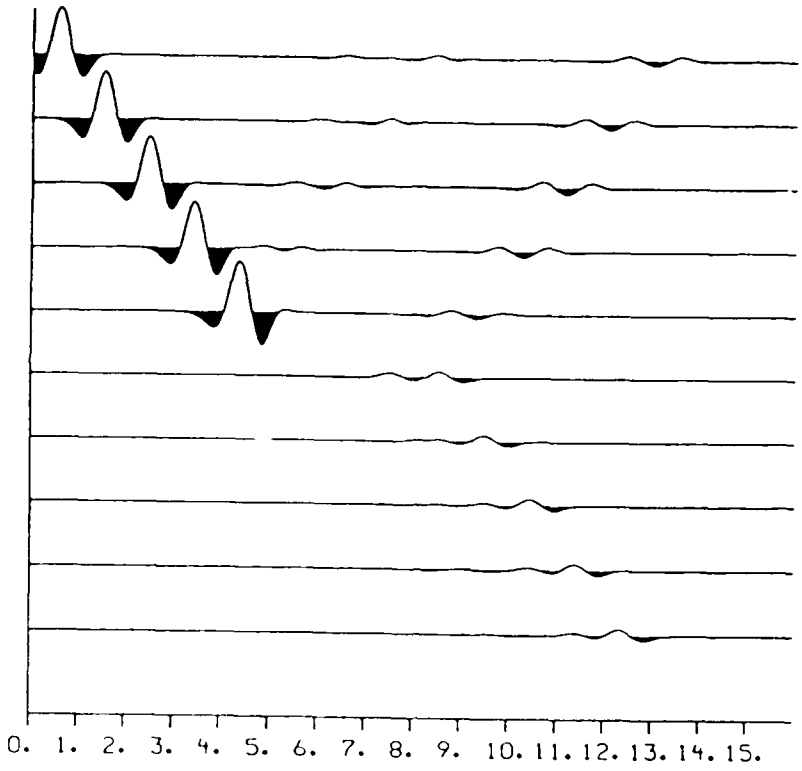
0. 1. 2. 3. 4. 5. 6. 7. 8. 9. 10. 11. 12. 13. 14. 15.
SURFACE VERT. R WAVE. 6.4km DOWNHILL

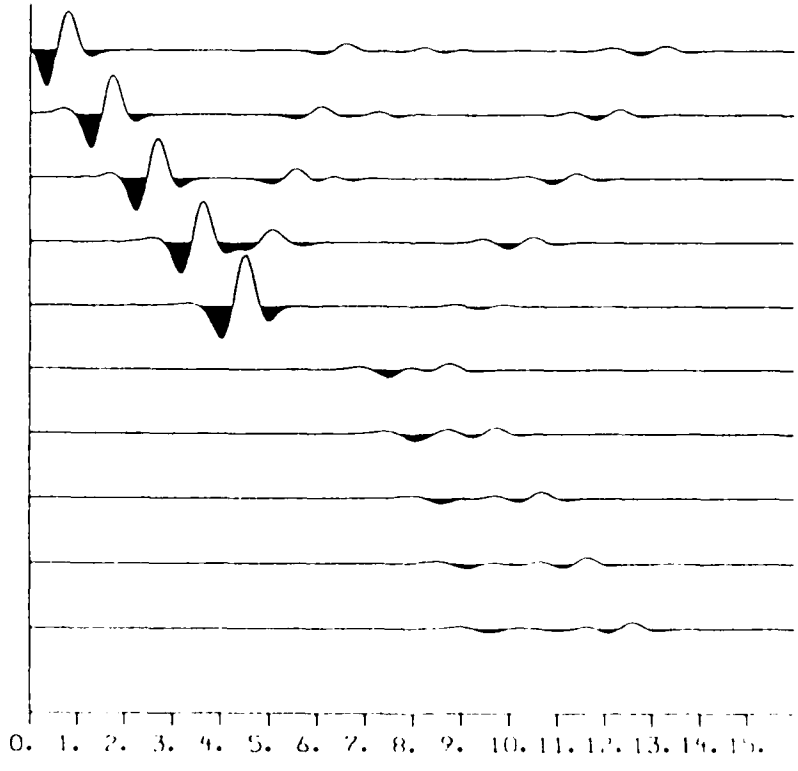
0. 1. 2. 3. 4. 5. 6. 7. 8. 9. 10. 11. 12. 13. 14. 15.
SURFACE HORI. R WAVE. 6.4km DOWNHILL

Figure 9A

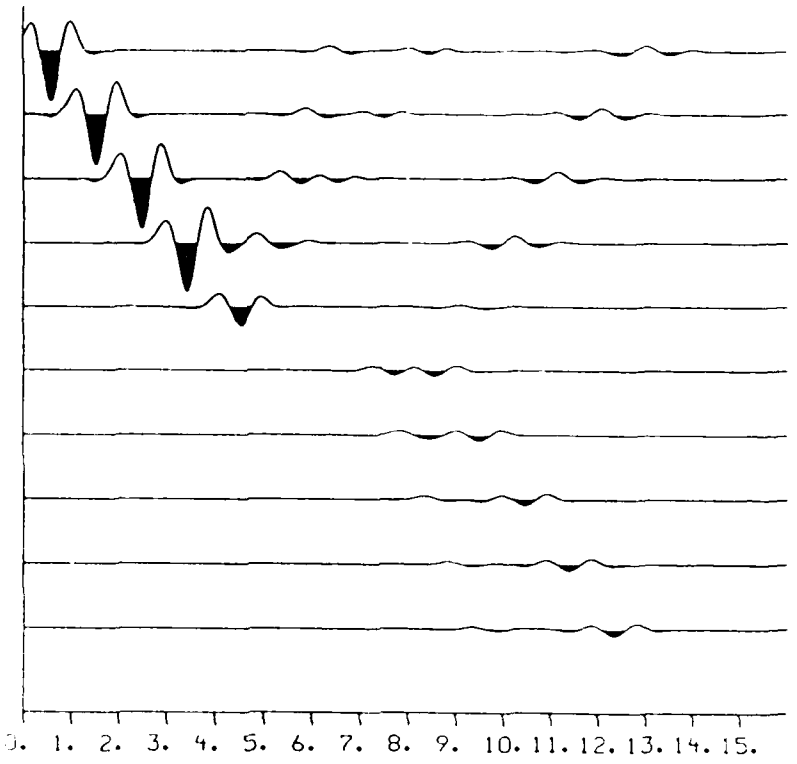
0. 1. 2. 3. 4. 5. 6. 7. 8. 9. 10. 11. 12. 13. 14. 15.
SURFACE DILA. R WAVE. 6.4km DOWNHILL

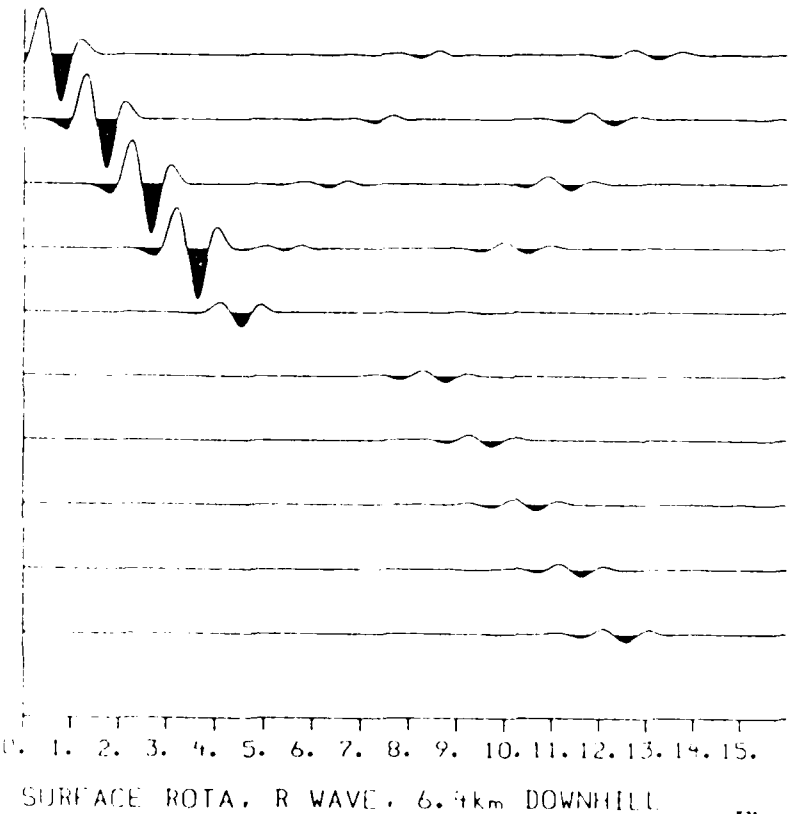
0. 1. 2. 3. 4. 5. 6. 7. 8. 9. 10. 11. 12. 13. 14. 15.
SURFACE ROTA. R WAVE. 6.4km DOWNHILL

Figure 9B

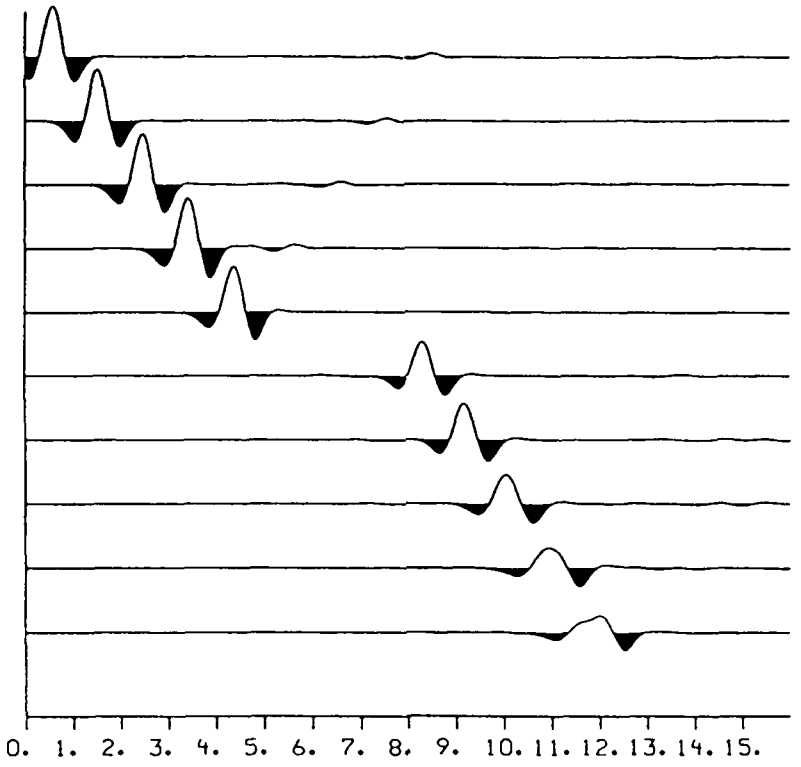
0. 1. 2. 3. 4. 5. 6. 7. 8. 9. 10. 11. 12. 13. 14. 15.
SURFACE VERT. R WAVE. 6.4km UPHILL

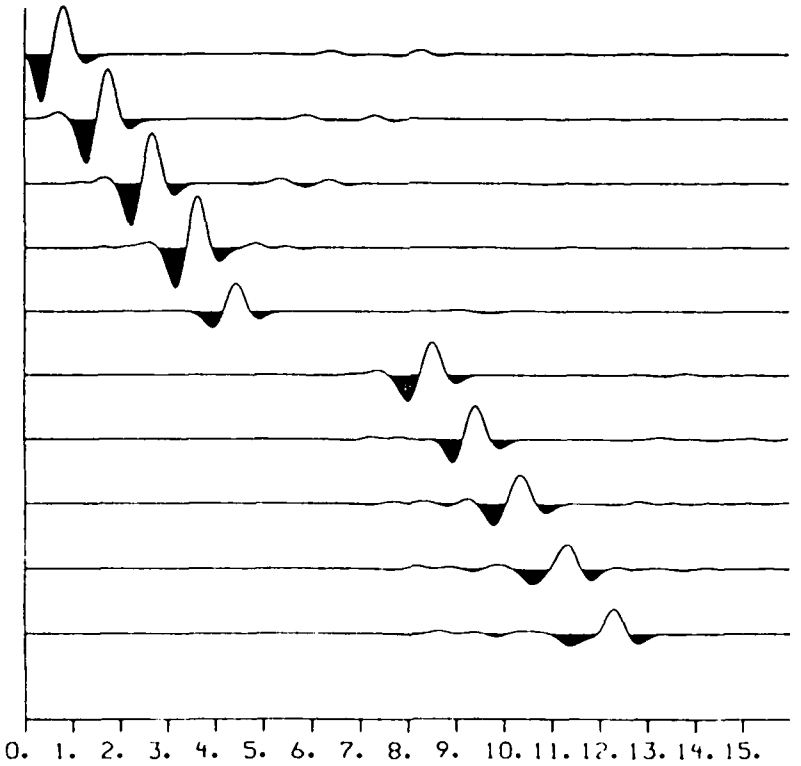
0. 1. 2. 3. 4. 5. 6. 7. 8. 9. 10. 11. 12. 13. 14. 15.
SURFACE HORI. R WAVE. 6.4km UPHILL

Figure 10A

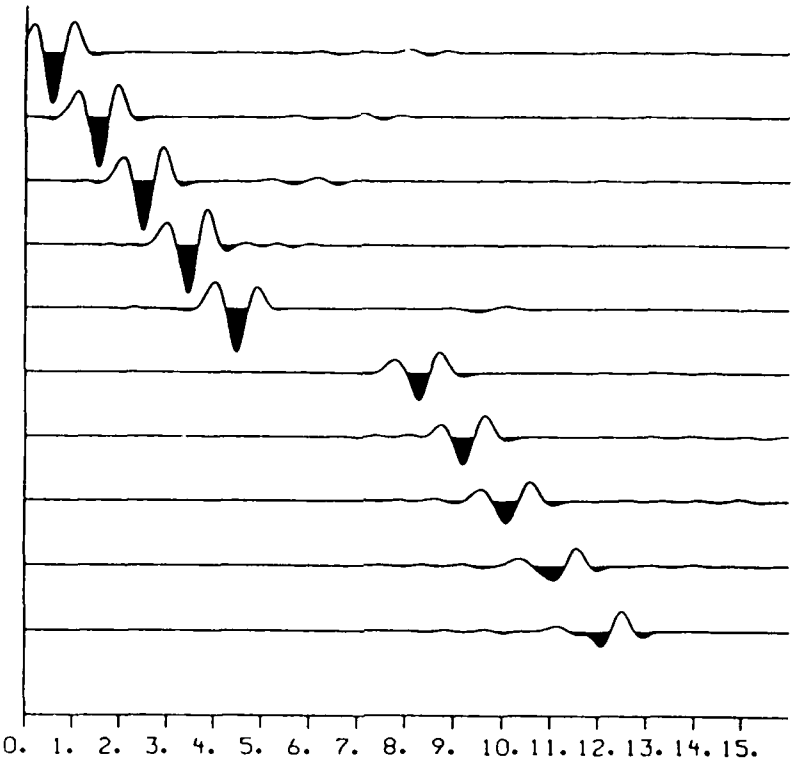
0. 1. 2. 3. 4. 5. 6. 7. 8. 9. 10. 11. 12. 13. 14. 15.
SURFACE DILA. R WAVE. 6.4km UPHILL

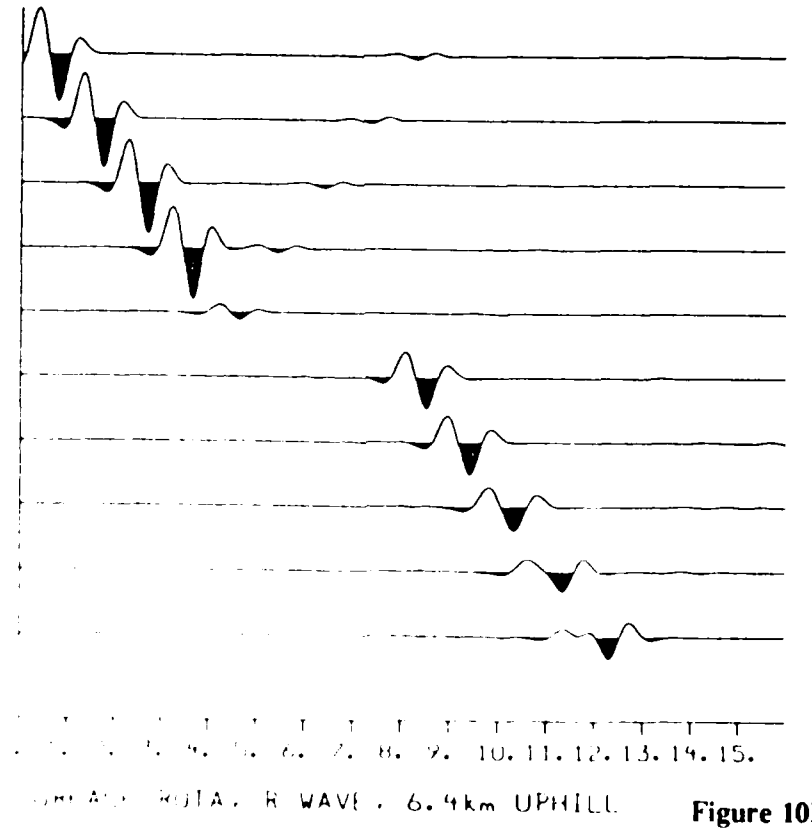
10. 11. 12. 13. 14. 15.
R WAVE . 6.4km UPHILL

Figure 10B

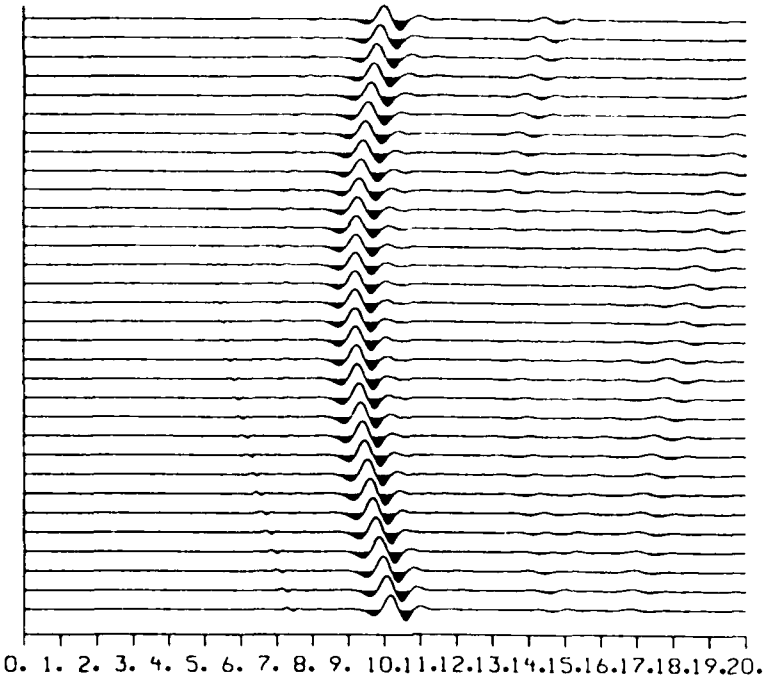
0. 1. 2. 3. 4. 5. 6. 7. 8. 9. 10.11.12.13.14.15.16.17.18.19.20.
R=>P(1km apart).R WAVE.1.6km DOWNHILL

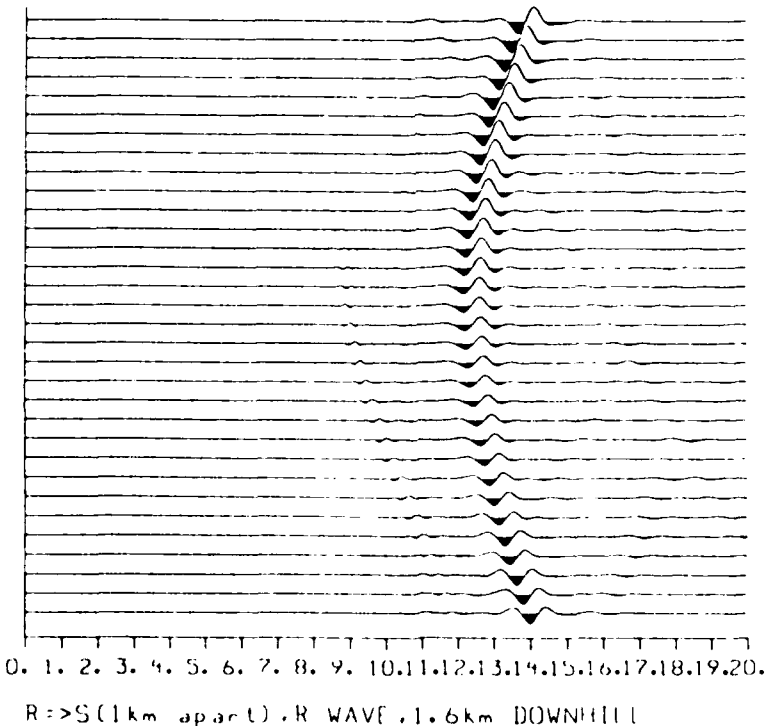
0. 1. 2. 3. 4. 5. 6. 7. 8. 9. 10.11.12.13.14.15.16.17.18.19.20.
R=>S(1km apart).R WAVE.1.6km DOWNHILL

Figure 11

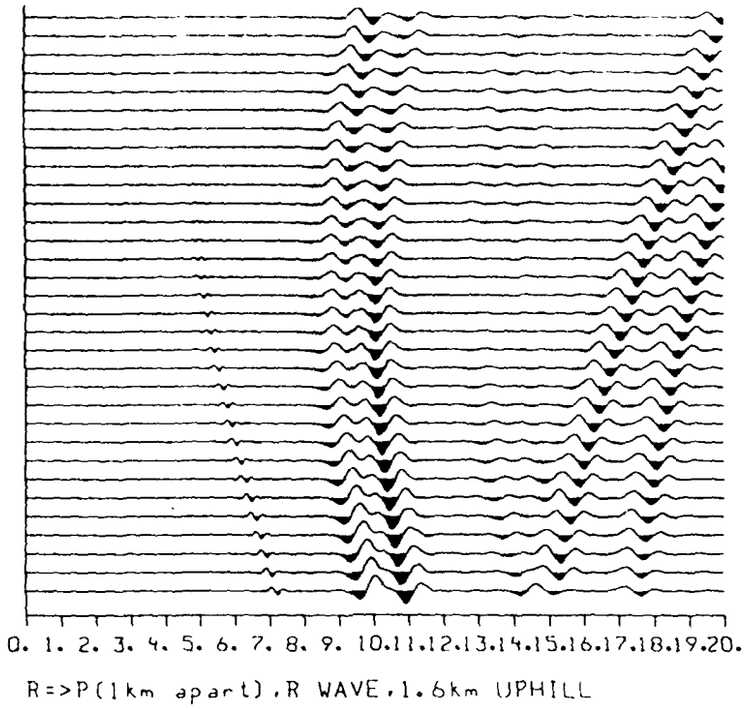
0. 1. 2. 3. 4. 5. 6. 7. 8. 9. 10.11.12.13.14.15.16.17.18.19.20.
R=>P(1km apart),R WAVE,1.6km UPHILL

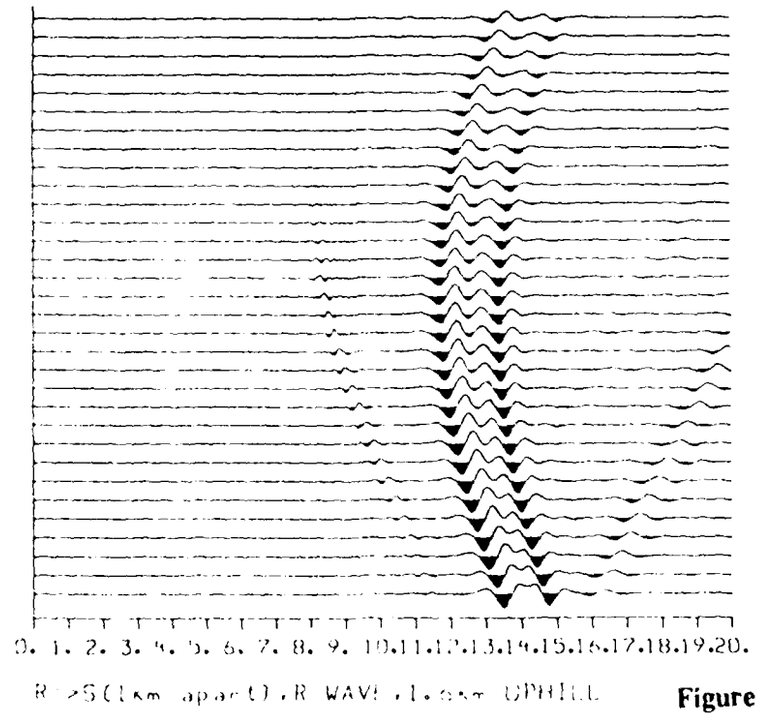
0. 1. 2. 3. 4. 5. 6. 7. 8. 9. 10.11.12.13.14.15.16.17.18.19.20.
R=>S(1km apart),R WAVE,1.6km UPHILL

Figure 12

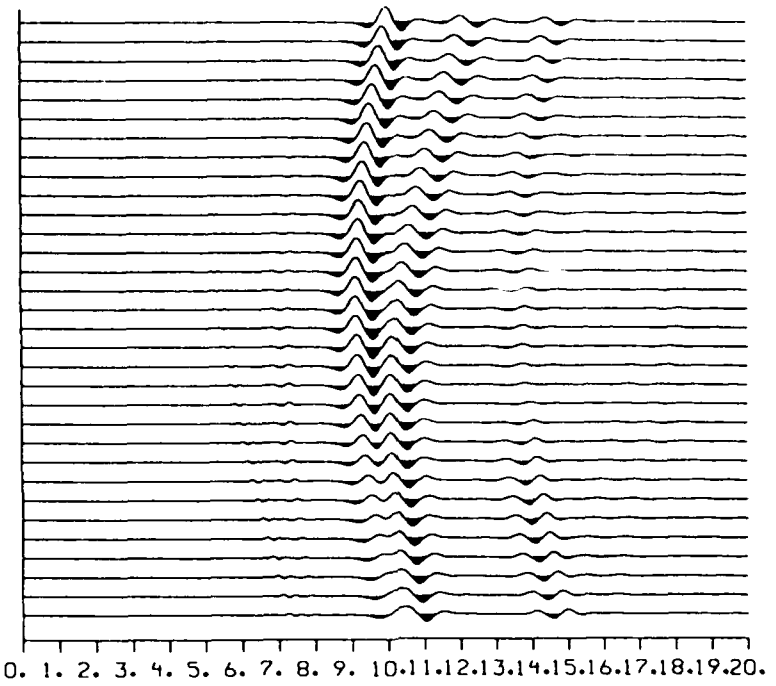
0. 1. 2. 3. 4. 5. 6. 7. 8. 9. 10.11.12.13.14.15.16.17.18.19.20.
R=>P(1km apart),R WAVE,6.4km DOWNHILL

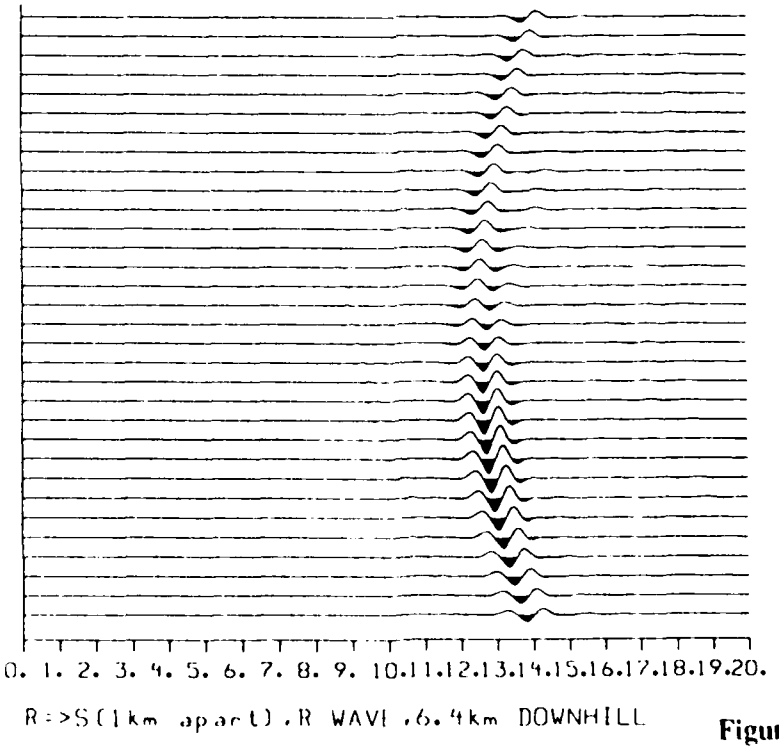
0. 1. 2. 3. 4. 5. 6. 7. 8. 9. 10.11.12.13.14.15.16.17.18.19.20.
R=>S(1km apart),R WAVE,6.4km DOWNHILL

Figure 13

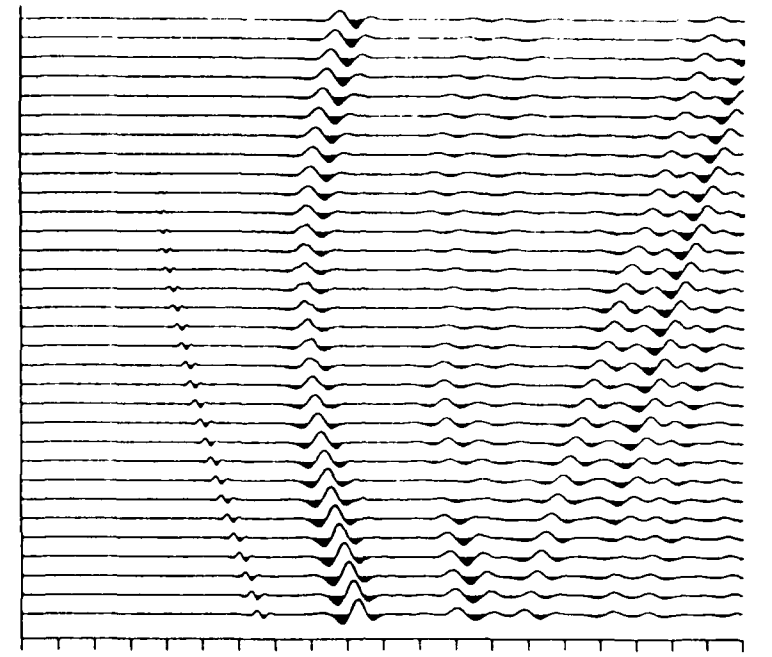
0. 1. 2. 3. 4. 5. 6. 7. 8. 9. 10.11.12.13.14.15.16.17.18.19.20.
R=>P(1km apart),R WAVE,6.4km UPHILL

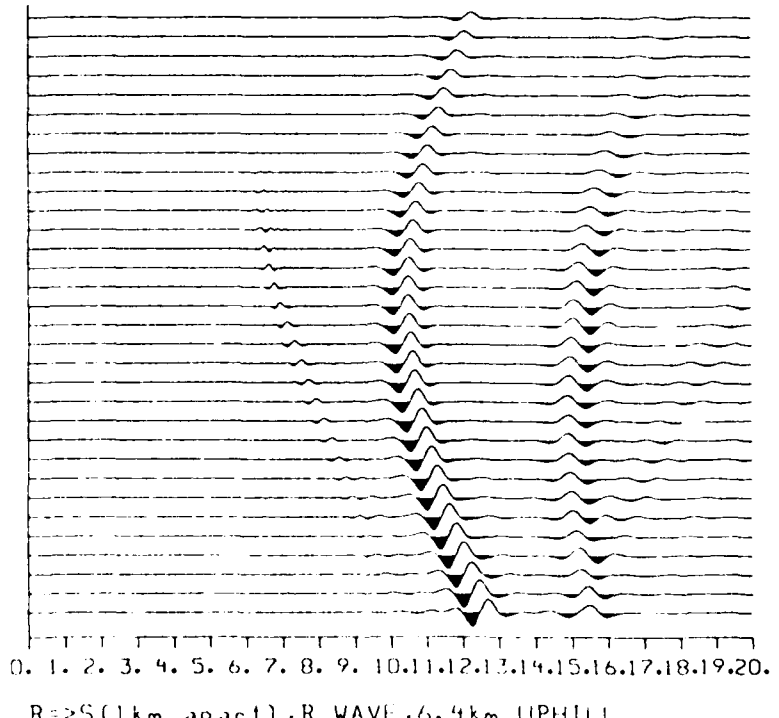
0. 1. 2. 3. 4. 5. 6. 7. 8. 9. 10.11.12.13.14.15.16.17.18.19.20.
R=>S(1km apart),R WAVE,6.4km UPHILL

Figure 14

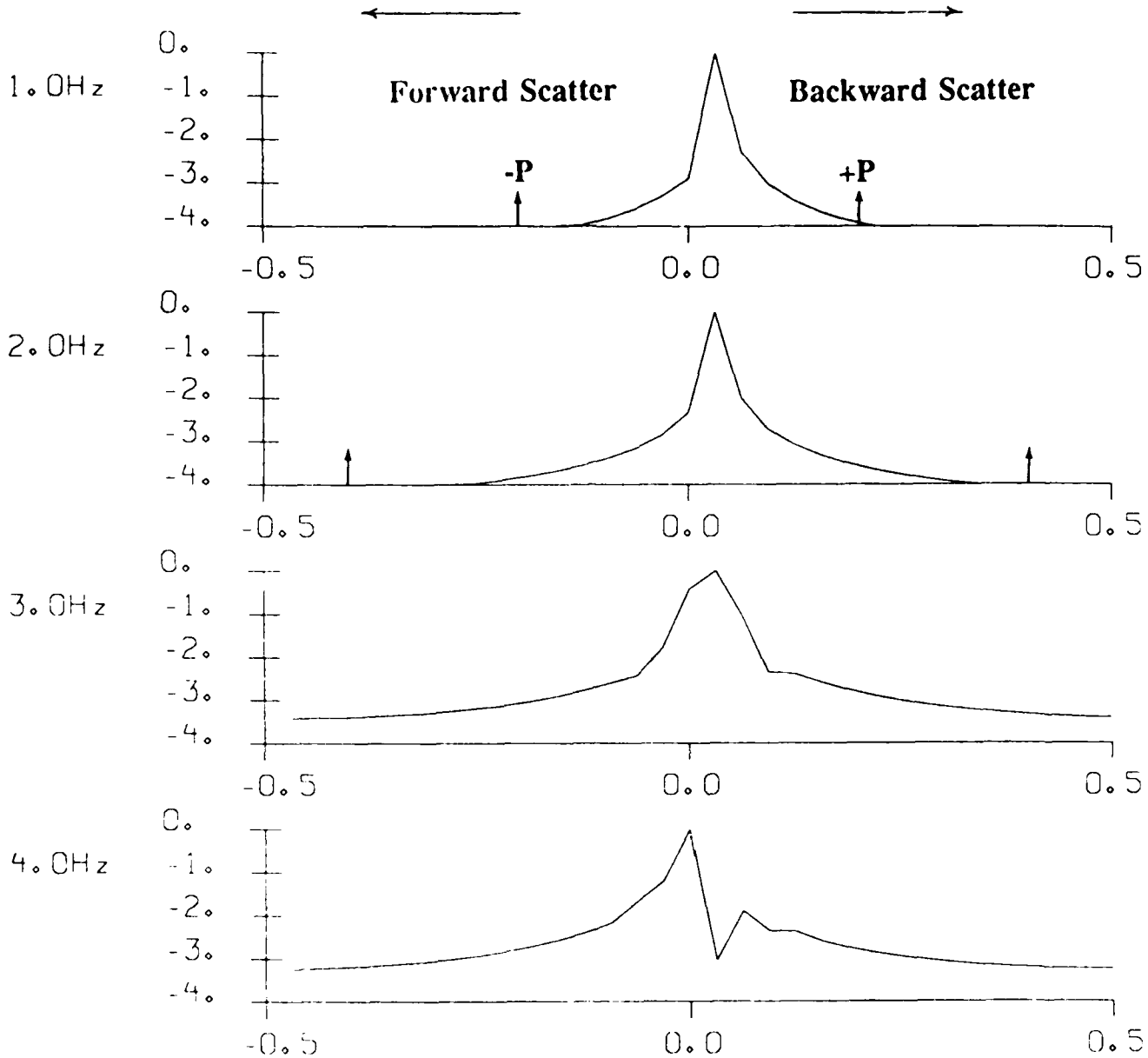
Forward Scatter
Backward Scatter
-P
+P
1.0Hz
2.0Hz
3.0Hz
4.0Hz
0.
-1.
-2.
-3.
-4.
-0.5
0.0
0.5
NORMALIZED Log(POWER) WAVENUMBER SPECTRA

Figure 15A

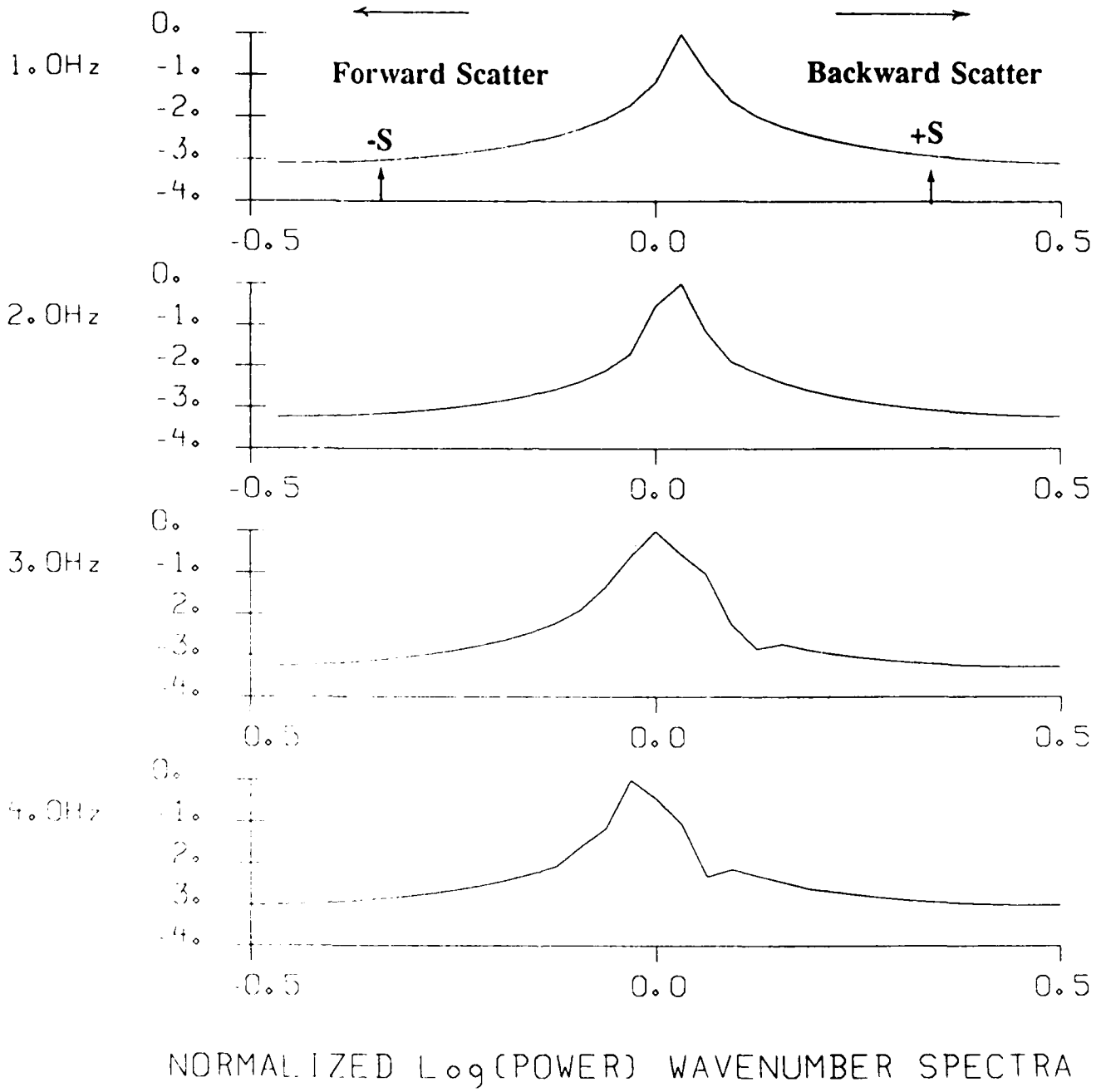
1.0Hz
2.0Hz
3.0Hz
4.0Hz
0.
-1.
-2.
-3.
-4.
Forward Scatter
Backward Scatter
-S
+S
-0.5
0.0
0.5
NORMALIZED Log(POWER) WAVENUMBER SPECTRA

Figure 15B

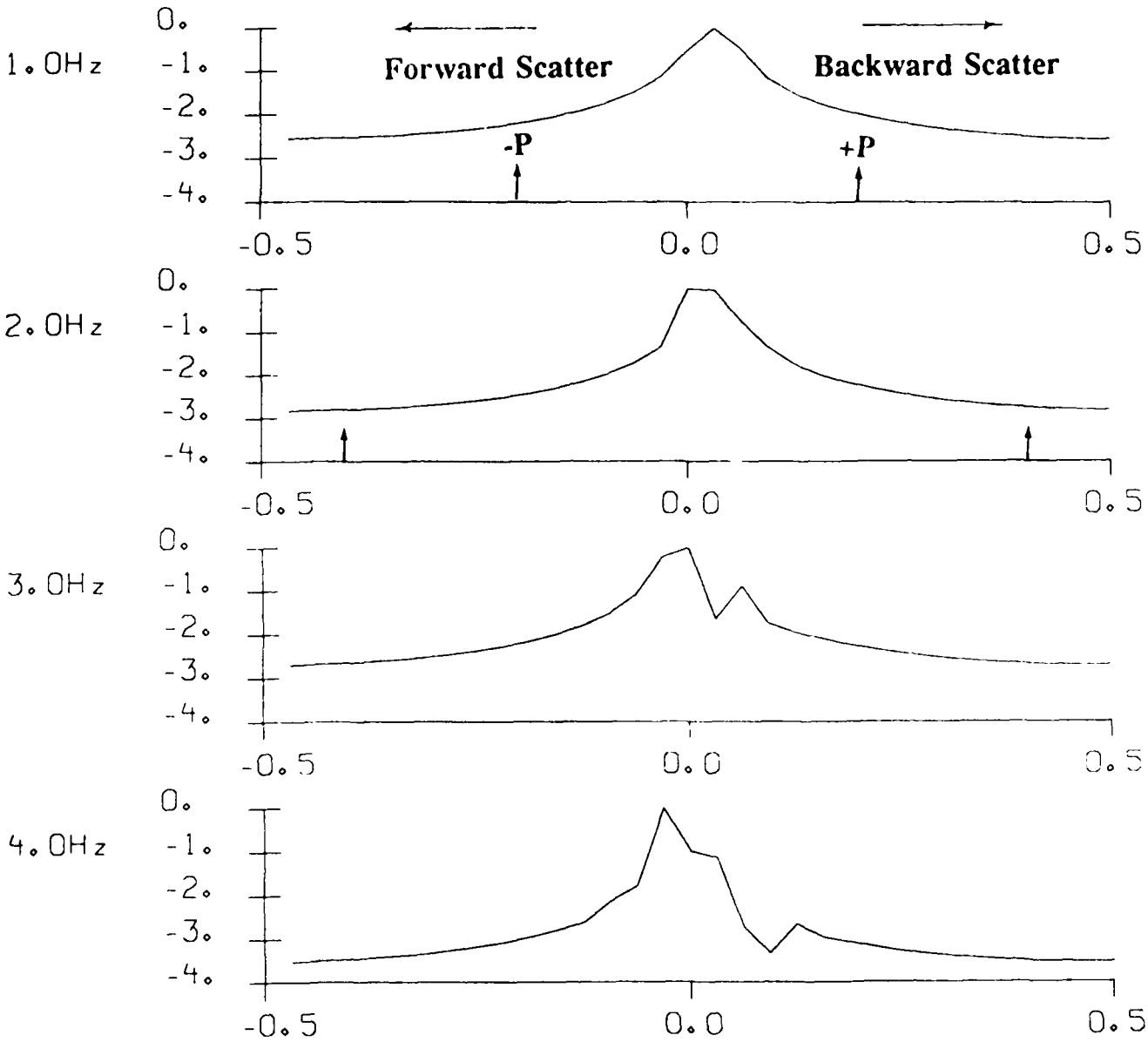
1.0Hz
2.0Hz
3.0Hz
4.0Hz
0.
-1.
-2.
-3.
-4.
Forward Scatter
Backward Scatter
-P
+P
-0.5
0.0
0.5
NORMALIZED Log(POWER) WAVENUMBER SPECTRA

Figure 16A

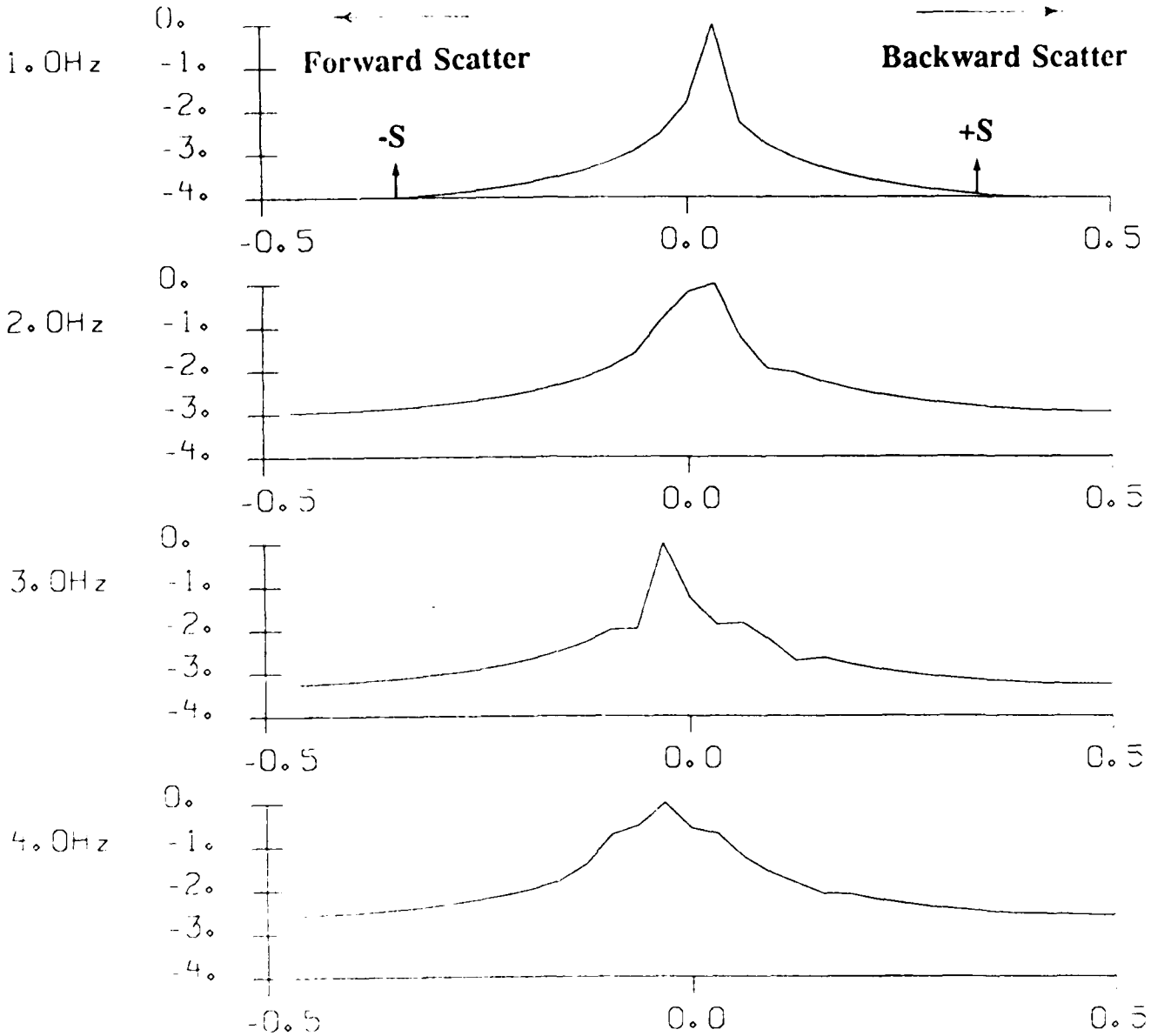
1.0Hz
2.0Hz
3.0Hz
4.0Hz
0.
-1.
-2.
-3.
-4.
Forward Scatter
Backward Scatter
-S
+S
-0.5
0.0
0.5
NORMALIZED Log(POWER) WAVENUMBER SPECTRA

Figure 16B

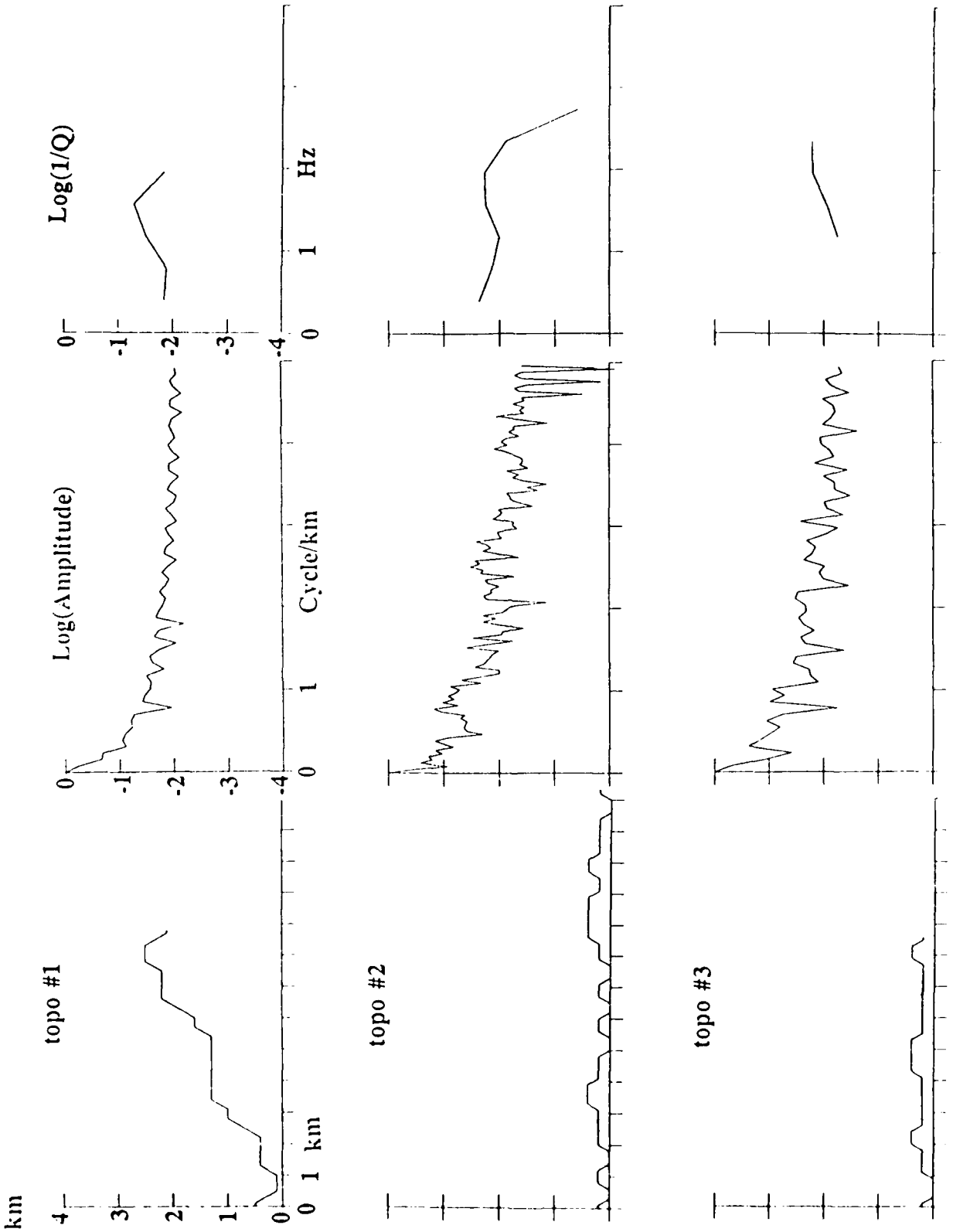
km
4
3
2
1
0
0 1 km
topo #1
Log(Amplitude)
0
-1
-2
-3
-4
0 1 Cycle/km
Log(1/Q)
0
-1
-2
-3
-4
0 1 Hz
topo #2
topo #3

Figure 17A

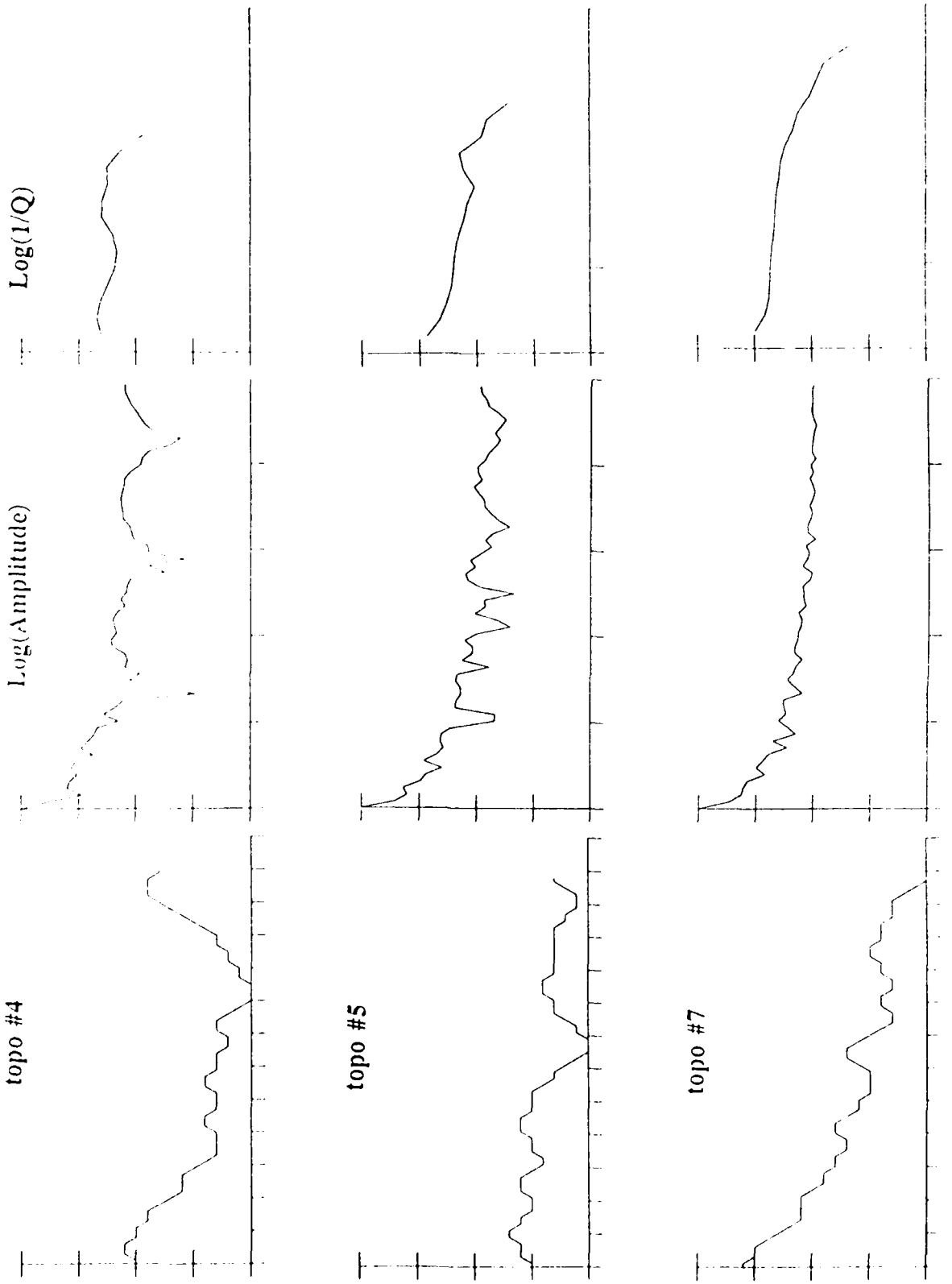

Figure 17B

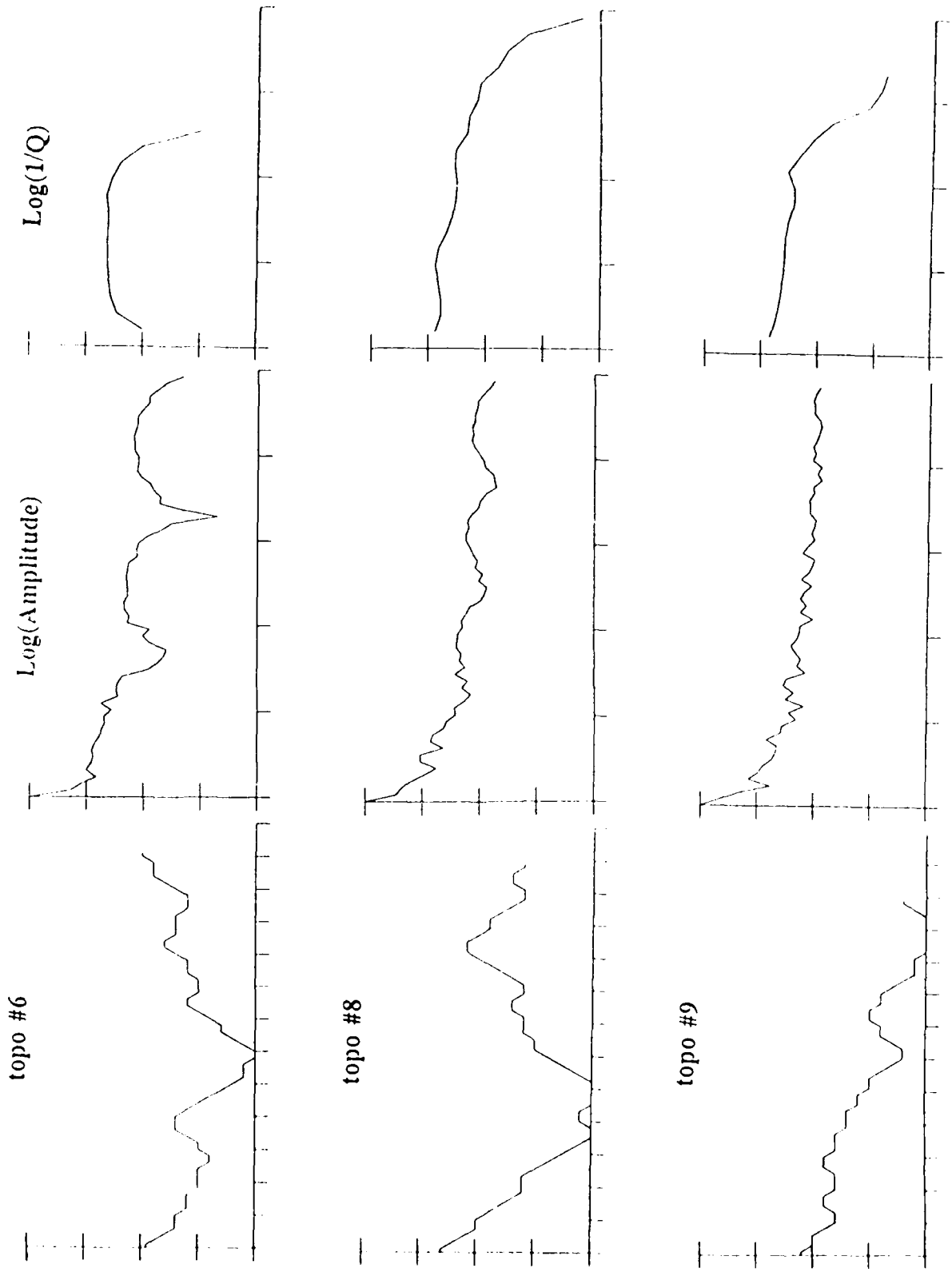

Figure 17C

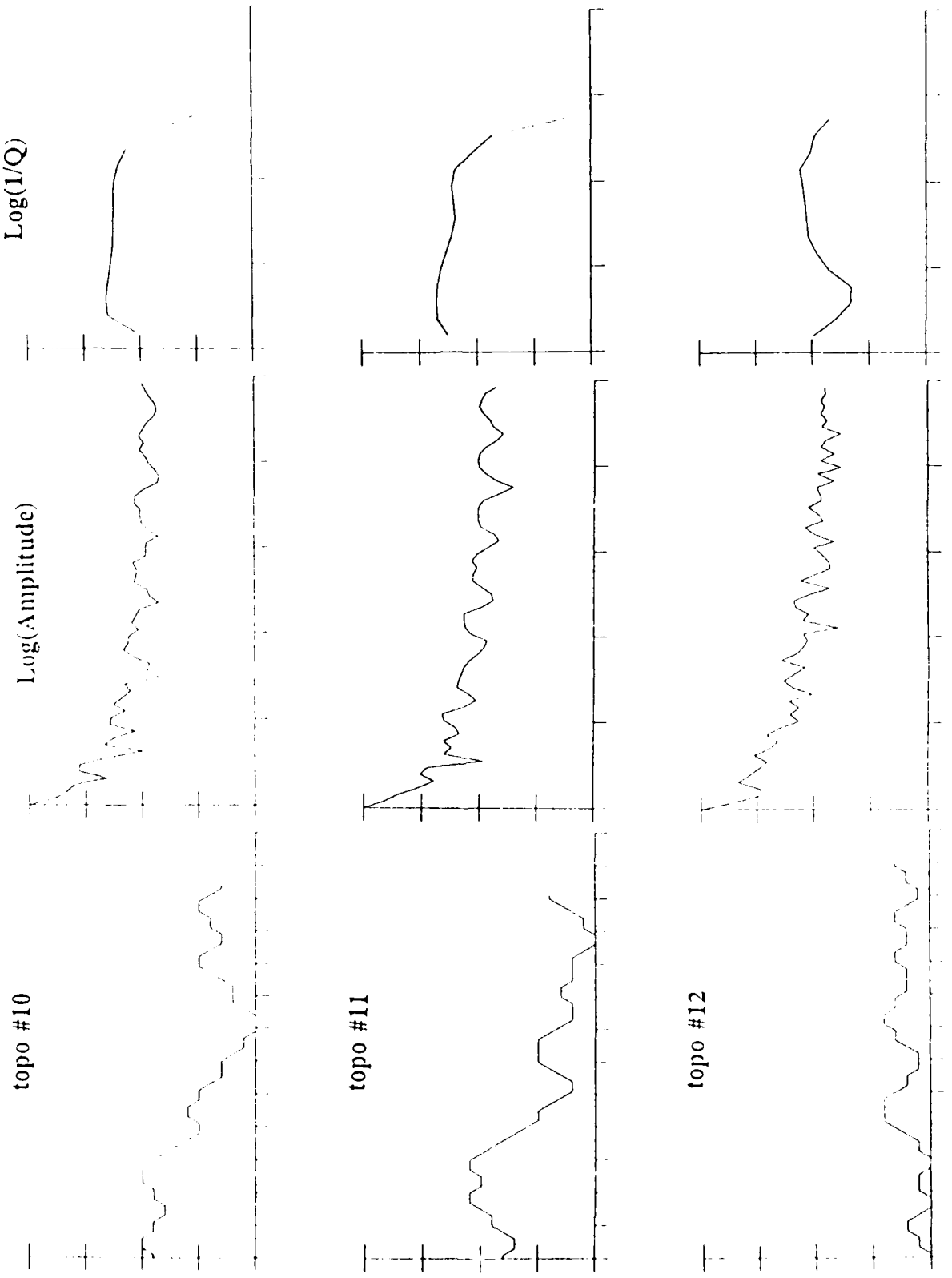

Figure 17D

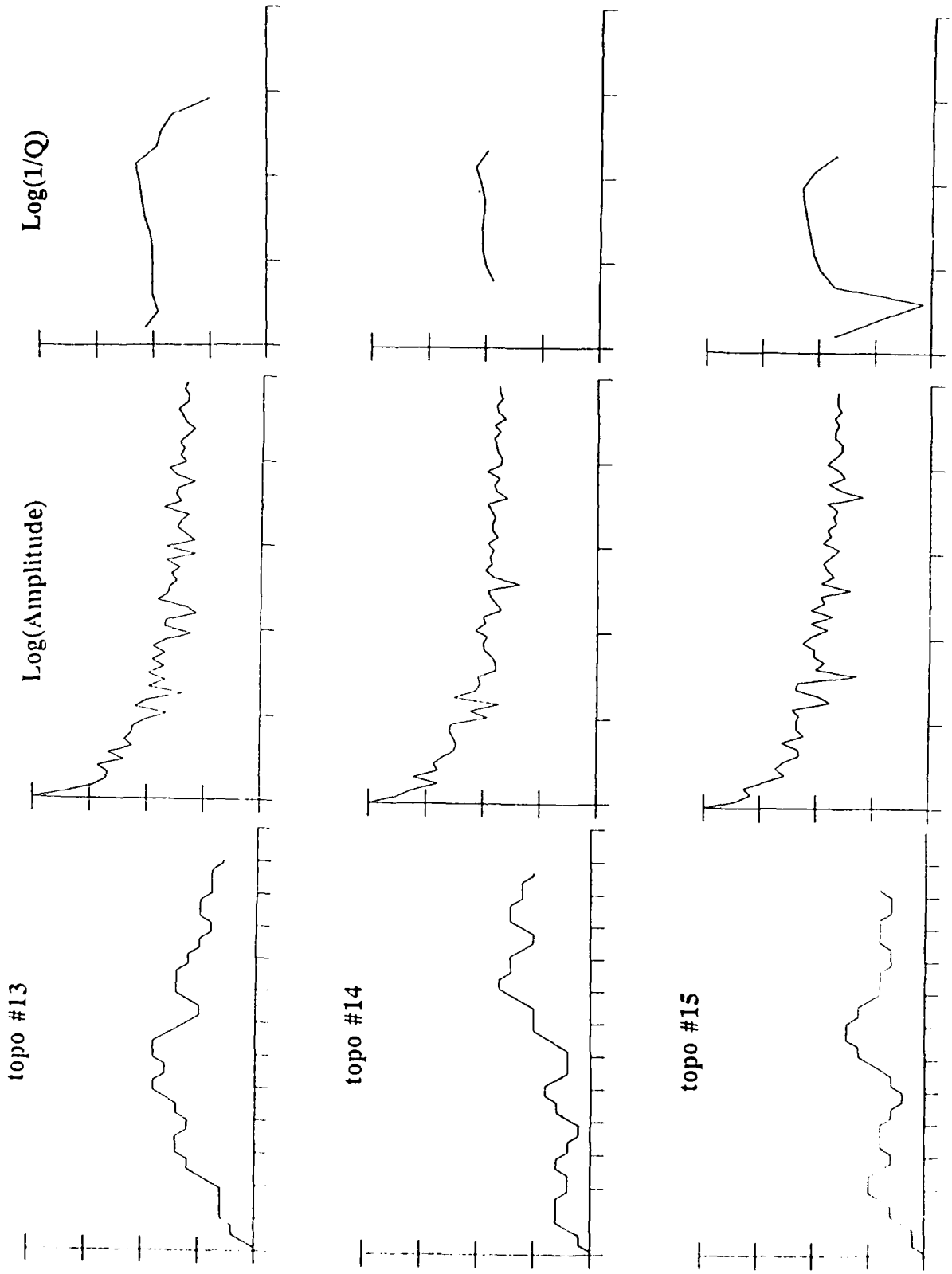

Figure 17E

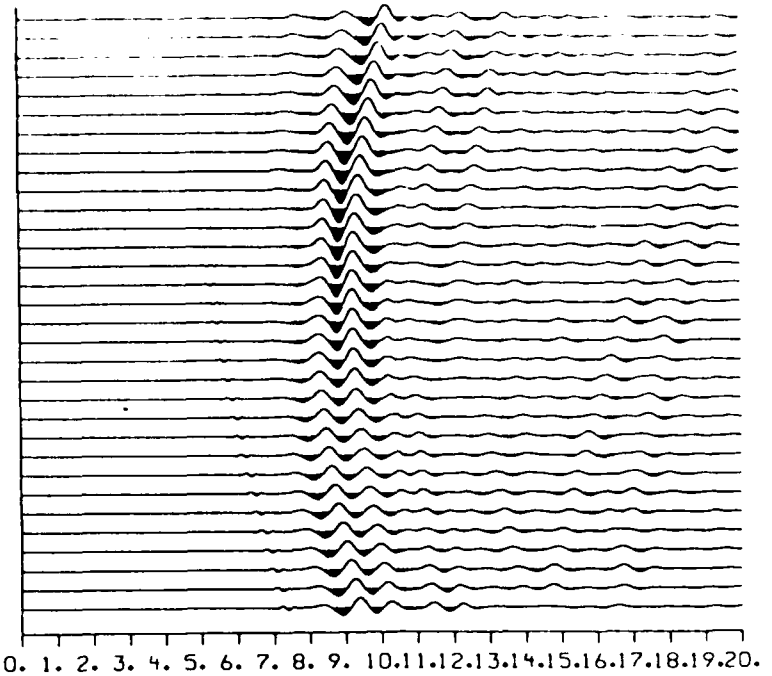
0. 1. 2. 3. 4. 5. 6. 7. 8. 9. 10.11.12.13.14.15.16.17.18.19.20.
R=>P, 1km apart, #5

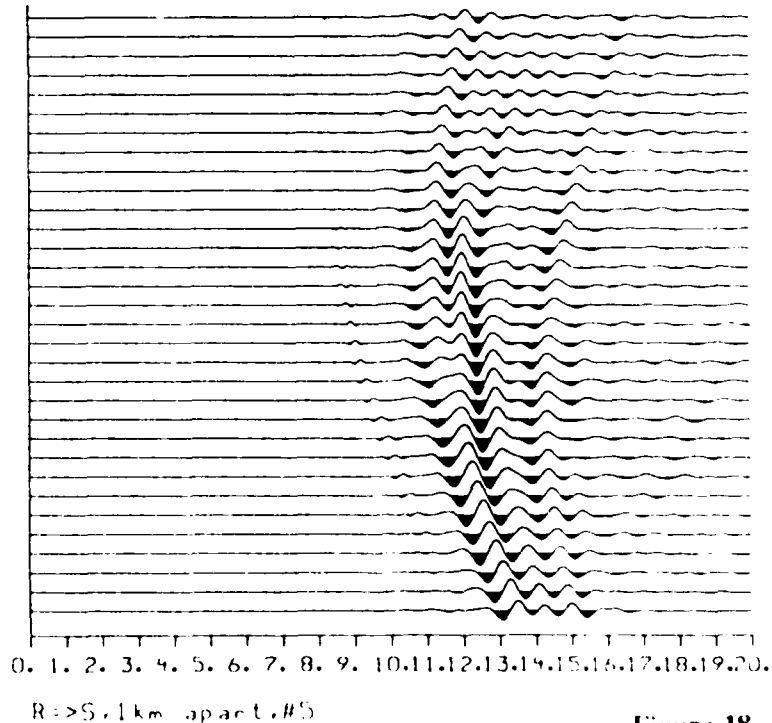
0. 1. 2. 3. 4. 5. 6. 7. 8. 9. 10.11.12.13.14.15.16.17.18.19.20.
R=>S, 1km apart, #5

Figure 18

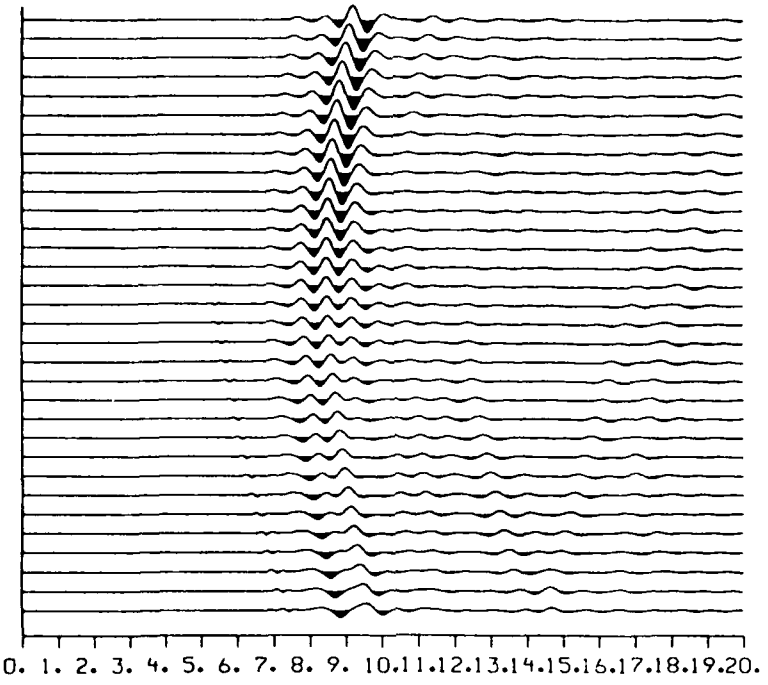
0. 1. 2. 3. 4. 5. 6. 7. 8. 9. 10.11.12.13.14.15.16.17.18.19.20.
R=>P,1km apart,#10

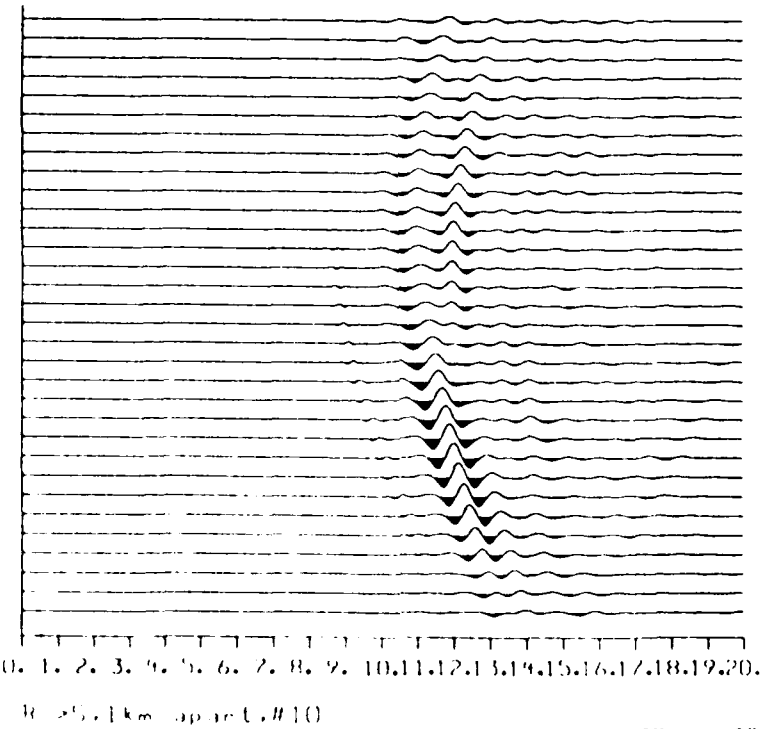
0. 1. 2. 3. 4. 5. 6. 7. 8. 9. 10.11.12.13.14.15.16.17.18.19.20.

Figure 19

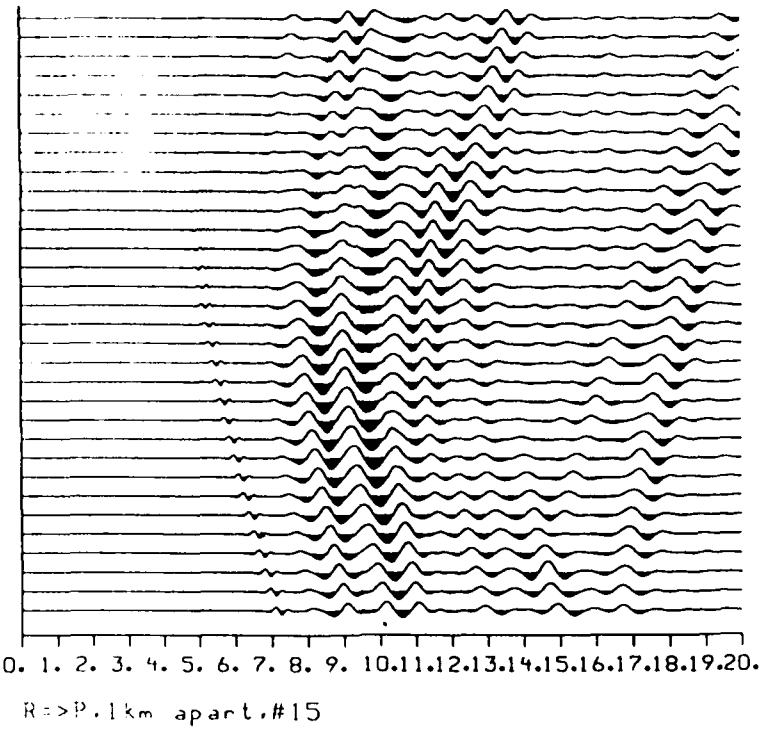
0. 1. 2. 3. 4. 5. 6. 7. 8. 9. 10.11.12.13.14.15.16.17.18.19.20.
R=>P, 1km apart, #15

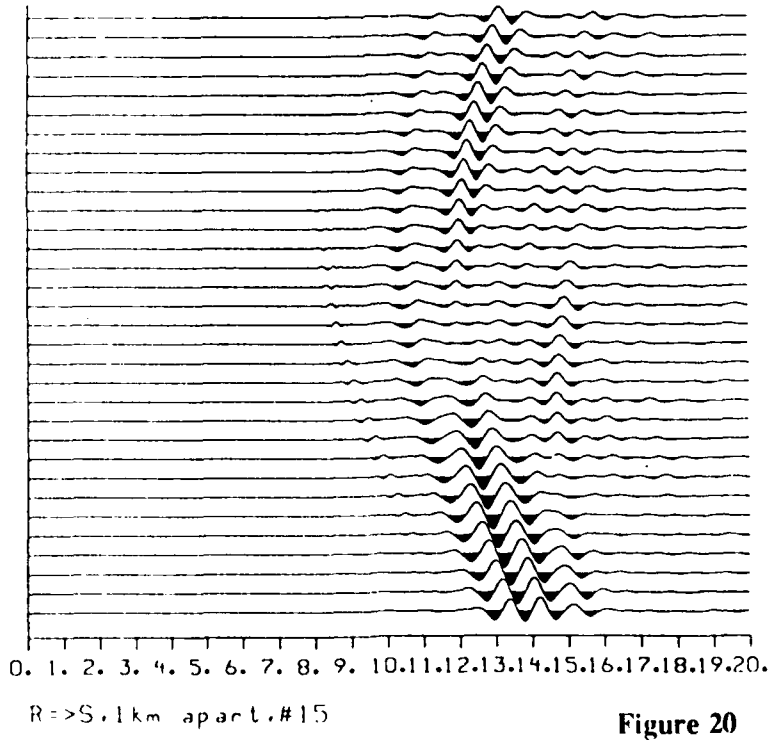
0. 1. 2. 3. 4. 5. 6. 7. 8. 9. 10.11.12.13.14.15.16.17.18.19.20.
R=>S, 1km apart, #15

Figure 20

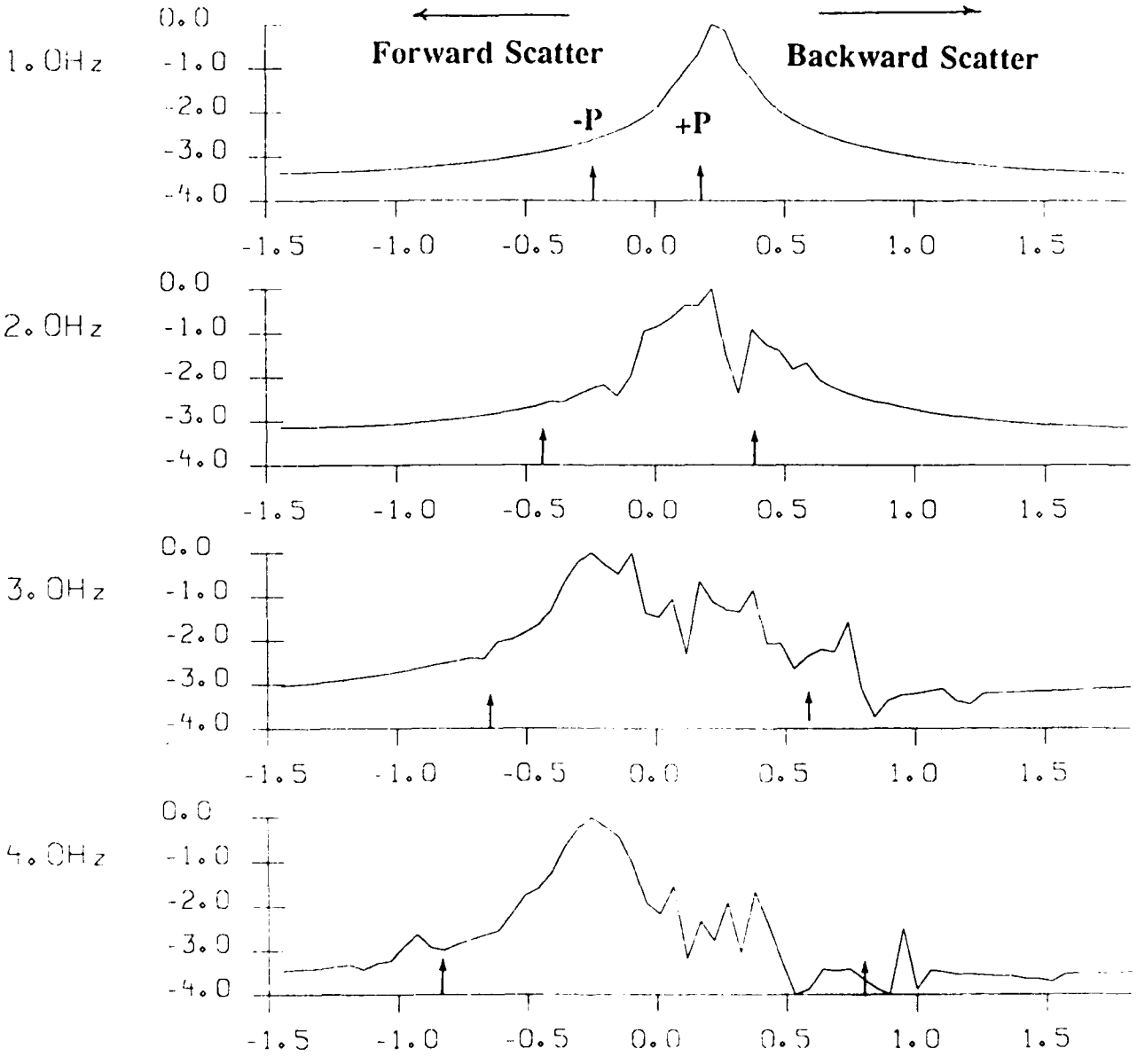
1.0Hz
2.0Hz
3.0Hz
4.0Hz
Forward Scatter
Backward Scatter
-P
+P
0.0
-1.0
-2.0
-3.0
-4.0
-1.5
-1.0
-0.5
0.0
0.5
1.0
1.5
NORMALIZED Log(POWER) WAVENUMBER SPECTRA

Figure 21A

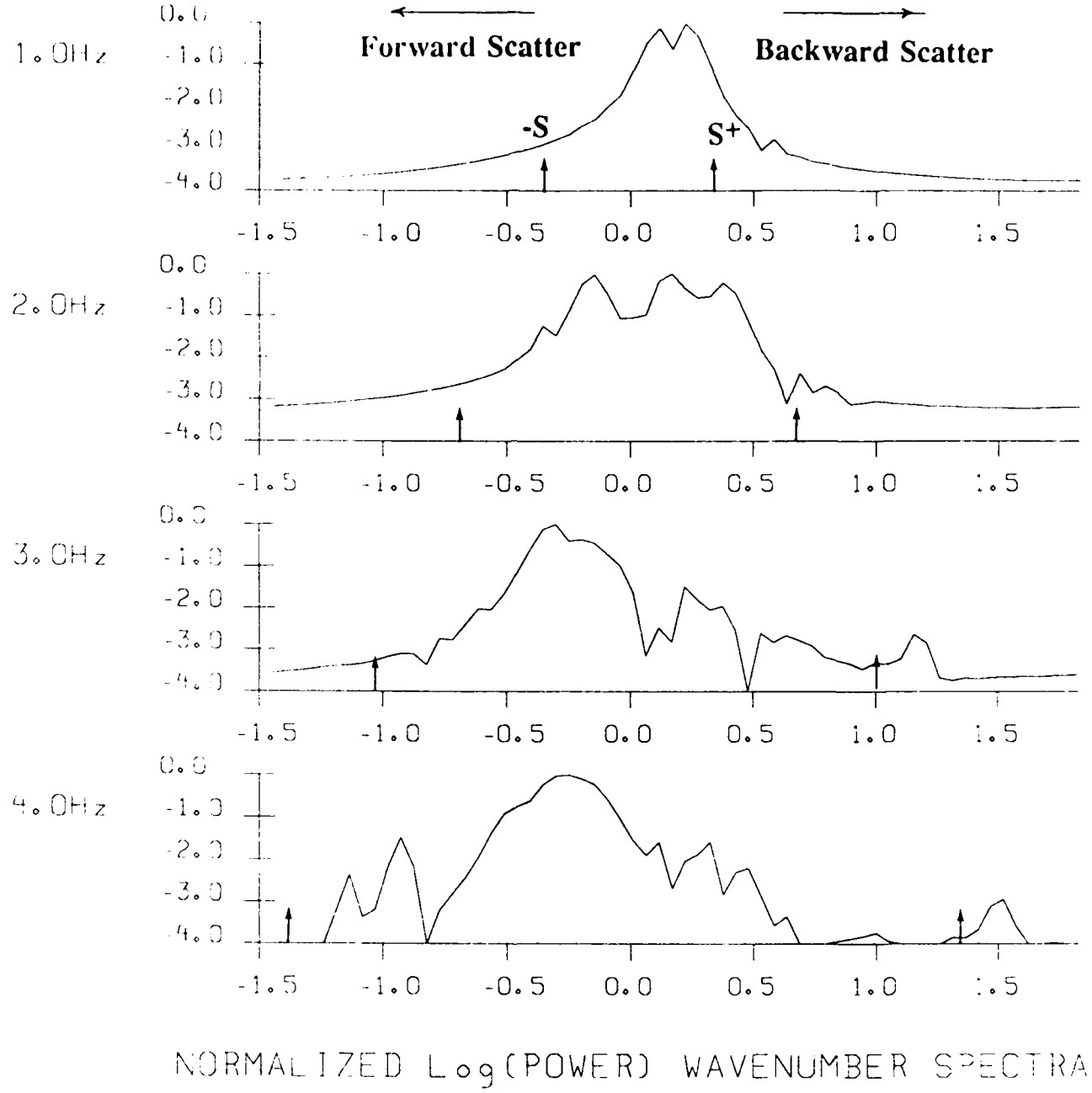
Forward Scatter
Backward Scatter
-S
S+
1.0Hz
2.0Hz
3.0Hz
4.0Hz
0.0
-1.0
-2.0
-3.0
-4.0
-1.5
-1.0
-0.5
0.0
0.5
1.0
1.5
NORMALIZED Log(POWER) WAVENUMBER SPECTRA

Figure 21B

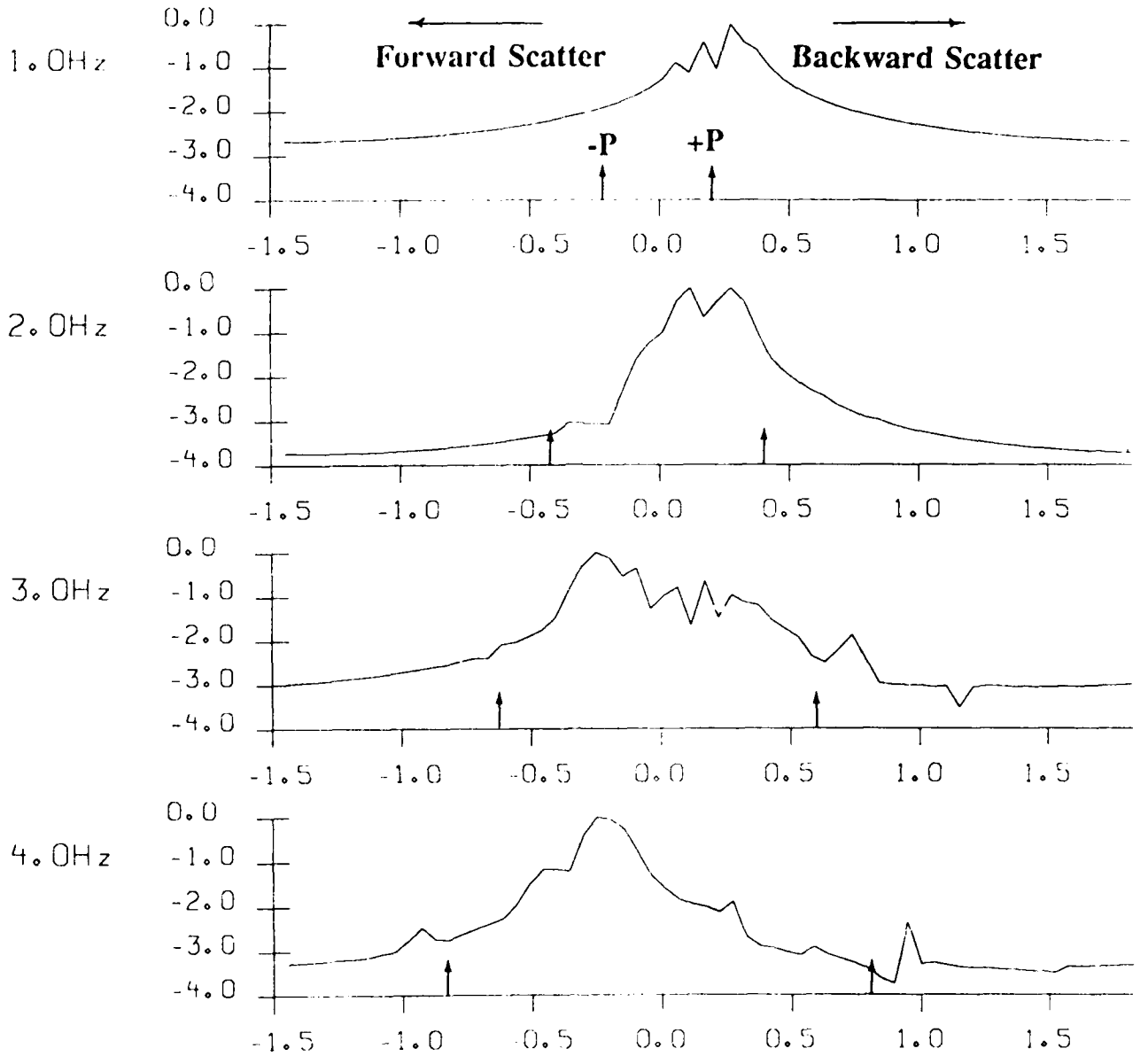
1.0Hz
2.0Hz
3.0Hz
4.0Hz
Forward Scatter
Backward Scatter
-P
+P
0.0
-1.0
-2.0
-3.0
-4.0
-1.5
-1.0
-0.5
0.0
0.5
1.0
1.5
NORMALIZED Log(POWER) WAVENUMBER SPECTRA

Figure 22A

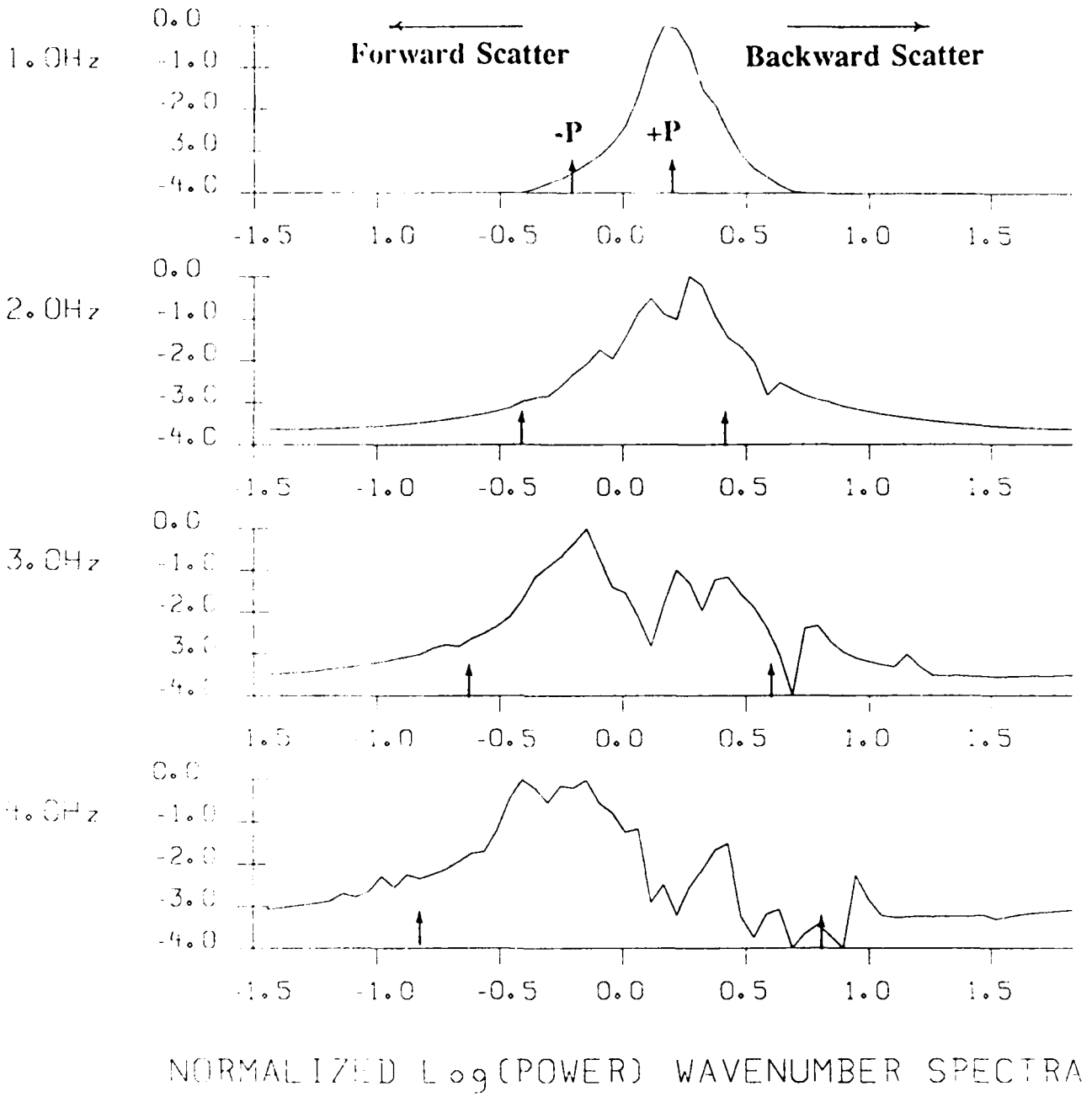
1.0Hz
2.0Hz
3.0Hz
4.0Hz
Forward Scatter
Backward Scatter
-P
+P
0.0
-1.0
-2.0
-3.0
-4.0
-1.5
-1.0
-0.5
0.0
0.5
1.0
1.5
NORMALIZED Log(POWER) WAVENUMBER SPECTRA

Figure 22B

END

5-87

DTIC